Pergamon

Geochimica et Cosmochimica Acta, Vol. 61, No. 7, p. 1541–1561, 1997

0016-7037/97 $17.00 + .00

PII S0016-7037(97)00004-5

Trace element disequilibria and magnesium isotope heterogeneity in 3655A: Evidence for a complex multi-stage evolution of a typical Allende Type B1 CAI

ALLEN K. KENNEDY,[1,2,*] JOHN R. BECKETT,[1] DAVID A. EDWARDS,[3,†] and IAN D. HUTCHEON[1,2,‡]

[1]Division of Geological and Planetary Sciences, California Institute of Technology, Pasadena, California 91125, USA
[2]Lunatic Asylum of the Charles Arms Laboratory, California Institute of Technology, Pasadena, California 91125, USA
[3]Division of Engineering and Applied Science, California Institute of Technology, Pasadena, California 91125, USA

(*Received July* 21, 1995; *accepted in revised form December* 19, 1996)

Abstract—We used the Panurge ion microprobe to measure concentrations of the rare earth elements (REEs), Ba, Hf, and Sr in melilite, clinopyroxene, plagioclase, and perovskite and Mg isotopes in plagioclase, spinel, melilite, fassaite, hibonite, grossular, and monticellite from the Allende Type B1 calcium-, aluminum-rich inclusion (CAI), USNM 3655A. The distribution and concentration of Ba and the REE in melilite from the melilite-rich mantle of 3655A are unlike those predicted from melilite-melt REE partitioning experiments for closed system crystal fractionation. REE concentrations are lower than expected in the first crystallized gehlenitic melilite, increase rapidly to higher than expected concentrations in melilite with intermediate åkermanite contents (Ak30–Ak40), and decrease as expected only during the late stage of mantle crystallization. Barium concentrations in melilite are 10–50 times those expected, and the LREE/HREE ratio increases continuously rather than remaining constant. The unexpected distribution of trace elements in melilite reflects a progressive enrichment of trace elements in the melt during the early stages of crystallization. A partial explanation for this observation is the dissolution of precursor perovskite that contained half or more of the total REE budget of the inclusion. In addition, there are large trace element enrichments adjacent to included spinel in melilite and similar but smaller enrichments adjacent to spinel in clinopyroxene. These enrichments are consistent with the existence of trace element enriched boundary layers at the mineral/melt interfaces. The fact that kinetic processes partially control trace element abundances and distributions suggests rapid cooling during crystallization of the melilite-rich mantle. Similar trace element signatures are ubiquitous in Type B1 CAI, suggesting that each experienced a similar thermal history.

The Mg isotope record of 3655A is distinguished by four salient features: (1) large ^{26}Mg excesses correlated with the respective Al/Mg ratios in plagioclase, melilite, and hibonite, (2) F_{Mg}, the mass-dependent fractionation of Mg, is positive, with enrichment of the heavier Mg isotopes in all primary phases, (3) a heterogeneous distribution of F_{Mg} values, with F_{Mg} in melilite systematically greater than in either spinel or fassaite, and (4) isotopically normal Mg in the secondary alteration phases, grossular and monticellite. The occurrence of $^{26}Mg^*$, the decay product of ^{26}Al, in anorthite implies early formation of 3655A, while ^{26}Al was extant at nearly the canonical solar system value of $\sim 5 \times 10^{-5}$. The trace element and Mg isotope heterogeneities suggest a formation scenario for 3655A which includes (1) flash heating to partially melt a solid precursor, (2) rapid cooling to allow survival of relict phases, (3) diffusive exchange of Mg between melilite and a nebular reservoir, and (4) alteration at low temperature. Although this model explains most of the trace element and isotopic characteristics of 3655A and other Type B1 CAIs, it does not provide an explanation for the rapid change of LREE/HREE ratios of melilite during crystallization. *Copyright © 1997 Elsevier Science Ltd*

1. INTRODUCTION

Type B1 CAIs are refractory inclusions, common to CV3 chondrites, that have a mantle formed by the axiolitic intergrowth of melilite crystals nucleated on the outer surface of the inclusion, surrounding a core of spinel, clinopyroxene, plagioclase, and melilite (MacPherson and Grossman, 1981). The inclusions crystallized from partial melts of pre-existing solids (Wark and Lovering, 1982; Stolper and Paque, 1986) and the abundances of trace elements in co-existing minerals provide information on thermal events prior to, during, and after the most recent melting event. It is important to characterize the evolution of Type B1 CAIs, as much of our information on the age of the solar system (Chen and Wasserburg, 1981), the presence of extinct radiogenic nuclides (Hutcheon, 1982; Podosek et al., 1991), and the occurrence of nucleosynthetic anomalies (Lee, 1988) comes from analyses of these objects. Although Type B1 CAIs have been studied extensively, some basic features of the distribution of trace elements remain unexplained. For example, Beckett et al. (1990) demonstrated experimentally that concentrations of the trivalent rare earth elements (REEs) in melilite decrease continuously during fractional crystallization of melilite and spinel for slowly cooled Type B1 compositions, but MacPherson et al. (1989) and Kennedy et al. (1990) have shown that the distributions of REEs and Ba in melilite from the mantle of Type B1 CAIs do not match the predicted variations. Kennedy et al. (1990) also identified trace element enrichments adjacent to spinel in-

* *Present address:* Department of Applied Physics, Curtin University of Technology, Perth 6001, Australia.
† *Present address:* Department of Mathematics, University of Maryland, College Park, Maryland 20742-4015, USA.
‡ *Present address:* Lawrence Livermore National Laboratory, P. O. Box 808, Livermore, California 94551, USA.

cluded within clinopyroxene and melilite not expected on the basis of equilibrium partitioning. Similar enrichments adjacent to included phases were noted by Simon et al. (1990) and Davis et al. (1991; see Fig. 10). In addition, U and Th concentrations in Type B1 melilite have proved difficult to explain in terms of equilibrium partitioning (Johnson et al., 1988; Burnett et al., 1990), and Johnson et al. (1988) identified Ti-rich "hotspots" in melilite from Type B1 CAIs that appear uncorrelated with any other phase. All of the above observations imply that trace element abundances and distributions in Type B1 CAIs reflect processes more complicated than simple fractional crystallization from a homogeneous melt. Each of these unexplained features has implications for either the nature of precursor materials that underwent partial melting or the thermal path followed during and after melting and crystallization.

The search for primary condensates within CAIs has been pursued with vigor over the last decade. El Goresy et al. (1979) suggested that spinel framboids might be relict condensates. Similarly, Pt-group-element-enriched opaque assemblages have been interpreted as xenoliths (El Goresy et al., 1985; Armstrong et al., 1987), as have spinel-hibonite spherules and spinel-free "islands" containing melilite, pyroxene, and plagioclase (El Goresy et al., 1979, 1985; MacPherson et al., 1989). Individual grains of spinel (El Goresy et al., 1979; Stolper and Paque, 1986; Kennedy et al., 1990), perovskite (Stolper and Paque, 1986; Fahey et al., 1987), hibonite (Ireland et al., 1991; Beckett and Stolper, 1994), and pyroxene (Paque, 1990) have been interpreted as relict in some inclusions, including 3655A. Demonstrating conclusively that a given phase predated the last melting event has, however, proved difficult if there are no isotopic differences. For example, Kuehner et al. (1989b) vs. Simon et al. (1990) or Kennedy et al. (1990) vs. Paque (1990) reached divergent conclusions about the existence of relict crystals within the same inclusions. Post-crystallization processes such as alteration and subsolidus re-equilibration also affected the inclusions (Meeker et al., 1983; Barber et al., 1984; Meeker, 1995).

In this paper, we describe a detailed study of trace element and Mg isotope distributions in USNM 3655A, a Type B1 CAIs from Allende. We measured concentrations of the REEs, Ba, Hf, and Sr in melilite, plagioclase, clinopyroxene, and perovskite, together with Mg isotopic compositions of potentially relict minerals, to constrain the thermal evolution. We use the term "relict" in this work to describe any phase that survived the last melting event, and thus "relict" applies to nebular condensates as well as any refractory phases formed in previous crystallization or metamorphic episodes. Data from other Type B1 CAIs collected in this laboratory (Kennedy et al., 1988) and elsewhere (MacPherson et al., 1989; Simon et al., 1990) also allow us to examine the extent to which the processes that affected 3655A are common to other Type B1 inclusions. We show that the distribution of trace elements in 3655A was influenced by (1) an influx of REEs into the melt during the initial stages of crystallization that may be explained by dissolution of REE-rich relict material, most probably perovskite, and (2) the development of trace-element-enriched boundary layers in the melt during crystallization. Preliminary reports of the results described in this paper are given in Kennedy et al. (1988, 1990).

2. ANALYTICAL TECHNIQUES

A polished thin section of 3655A was examined by optical transmission and reflectance microscopy and by backscattered electron imaging using a JEOL JSM 35CF scanning electron microscope (SEM) with a Tracor TN 5500 energy dispersive system (EDS). The EDS analyses were reduced using a modified Bence-Albee procedure (Armstrong, 1982, 1984). EDS analyses were obtained before and after ion microprobe analyses to determine the major element composition of the analyzed region and to check for overlap of the ion microprobe beam onto adjacent phases. Three or four points were analyzed around each ion probe pit.

Trace element and Mg isotopic measurements were obtained using PANURGE, a modified IMS-3f ion microprobe. Magnesium isotope measurements were obtained using the operating conditions and procedures of Hutcheon et al. (1987). Mass-dependent fractionation is expressed as F_{Mg}, the permil deviation of the $^{25}Mg/^{24}Mg$ ratio from the value measured in a mineralogically similar terrestrial standard. Burma spinel, Miakejima plagioclase, Madagascar hibonite, Jeffery grossular, monticellite, and glasses of fassaitic pyroxene and melilite composition were used as Mg isotope standards (Table 1). Variations in $^{26}Mg/^{24}Mg$ are expressed as $\delta^{26}Mg$, the permil deviation relative to $^{26}Mg/^{24}Mg = 0.13955$ after normalizing to $^{25}Mg/^{24}Mg = 0.12663$ using a power law to correct for fractionation (Brigham, 1990). Uncertainties for F_{Mg} and $\delta^{26}Mg$ values given in the text and tables are two standard deviations of the mean, or two standard deviations of the measurements, and both incorporate uncertainties from analyses of standards. REEs, Ba, Sr, and Hf were measured using techniques and standards discussed in Kennedy and Hutcheon (1992). During analysis of perovskite, overlap of the ion beam onto surrounding melilite was monitored using Si^- or Al^+, and, in two instances, corrections were made for contamination. The corrections were, however, minor for these analyses (~5%) and only slightly larger than the uncertainty of the measurements, typically 2–5%.

3. PETROGRAPHY

Wark and Lovering (1982) and Paque (1990) give petrographic descriptions of 3655A. It is a Type B1 CAI with a melilite-rich mantle, zoned from gehlenitic (Ak5) melilite (mel) at the rim to akermanitic melilite (Ak66) at the core-mantle boundary of the inclusion. Figure 1 shows a portion of 3655A; the characteristic features of this Type B1 inclusion are clearly visible. The lower two-thirds of the photomicrograph shows the melilite-rich mantle composed of axiolitic melilite with minor spinel (sp). Part of the spinel-rich core of the inclusion containing clinopyroxene (cpx), a large spinel palisade (Wark and Lovering, 1982) near the core-mantle boundary, and a small palisade towards the rim of the inclusion are also visible. Opaque assemblages occur throughout the inclusion, and small (<20 μm) rounded perovskites (pv) are present near the outer edge (Fig. 2a).

Table 1. Magnesium isotope standards.

Sample	$\Delta^{25}Mg$ (‰)[1]	$\delta^{26}Mg$ (‰)[2]	$^{27}Al/^{24}Mg$
Melilite glass	−9.8 ± 0.5	−0.8 ± 1.4	6.3
Fassaite glass	−6.3 ± 0.3	0.5 ± 0.6	1.7
Burma spinel	−9.9 ± 0.4	0.2 ± 0.5	2.5
Madagascar hibonite	−8.2 ± 1.1	0.1 ± 2.2	34
Miakejima plagioclase	−1.8 ± 2.8	1.8 ± 3.2	380
Jeffery grossular	−5.4 ± 1.7	0.2 ± 2.4	91
Monticellite	−6.1 ± 0.8	−0.9 ± 1.5	0.01

[1] Deviation in permil from $^{25}Mg/^{24}Mg = 0.12663$

[2] Deviation in permil from $^{26}Mg/^{24}Mg = 0.13955$ after power-law mass-fractionation correction (see text).

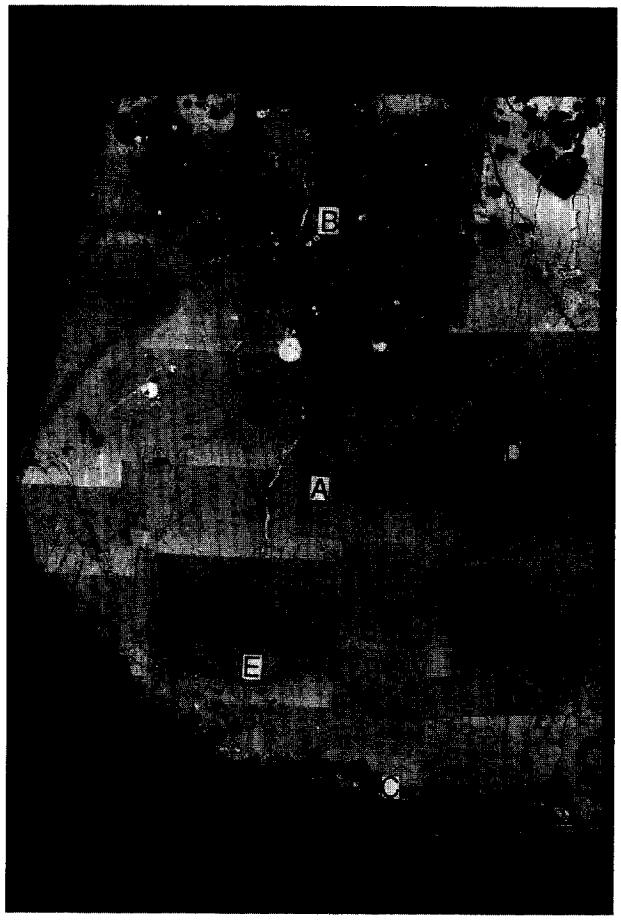

Fig. 1. Backscattered electron photomicrograph of a part of 3655A showing different regions and features that are labeled as follows: (A) melilite-rich mantle (Ion microprobe pits, representative examples of which are indicated by arrows, are visible along a traverse within a single mantle melilite crystal), (B) the spinel-rich core of the inclusion containing clinopyroxene, anorthite, and melilite, (C) the Wark-Lovering rim, (D) a large spinel palisade near the core-mantle boundary, and (E) a small spinel palisade towards the rim of the inclusion. Rounded high reflectivity objects are sulfide-rich opaque assemblages. Scale bar is 100 μm.

Perovskite sometimes occurs as a string of grains or as grains that appear to be adhering to a spinel palisade (Fig. 2a). In addition, there are vestiges of a Wark-Lovering rim sequence (Wark and Lovering, 1977) containing spinel and hibonite (hib). Spinel, opaque assemblages (El Goresy et al., 1979; Blum et al., 1989) and small (<10 μm) clinopyroxene grains are poikilitically enclosed within the mantle melilite. The core of the inclusion contains melilite, clinopyroxene, spinel, and plagioclase (plag). Some clinopyroxenes exhibit a patchy distribution of TiO_2 in their cores (see Figs. 1, 2 of Paque, 1990), and Paque (1990) has suggested that these cores may be relict.

Detailed petrographic descriptions of 3529Z and Egg 6 are presented elsewhere (Meeker et al., 1983; Meeker, 1990; Podosek et al., 1991). With the exception of a spinel free region in the core of 3529Z (Meeker, 1990), both inclusions are typical Type B1 CAIs with well-developed melilite-rich mantles, zoned from low (Ak $<$ 10) to high (Ak $>$ 55) akermanite contents, surrounding cores containing spinel, clinopyroxene, plagioclase, and melilite.

4. RESULTS

4.1. Rare Earth Elements

REE concentrations were measured in (1) traverses within individual melilite crystals extending from the edge of the inclusion to the core-mantle boundary, (2) short traverses approaching spinel included within melilite and clinopyroxene, (3) perovskite included within mantle melilite, both adjacent to the small spinel palisade of Fig. 1 (region E) and as isolated grains, (4) melilite and plagioclase in the core of the inclusion, and (5) traverses across the patchy core and overgrowth of high-Ca pyroxenes from the core of the inclusion and in a large normally zoned clinopyroxene at the core-mantle interface.

Trace element abundances in melilite, fassaite, plagioclase, and perovskite, mole fractions of akermanite in melilite, and the proportion of diopside and Ti pyroxene components in fassaite are given in Tables 2–4. Representative chondrite-normalized REE patterns are shown in Fig. 3. The REE pattern of melilite (Table 2; Fig. 3a) is either flat or light REE (LREE) enriched with La ranging from 1–50 $\times$ chondritic (ch) and the heavy REEs (HREEs) from 0.03–22 $\times$ ch. All of the melilite analyses are characterized by positive Eu anomalies. Both the size of the anomaly and the chondrite normalized LREE/HREE ratio are a function of position within the inclusion, ranging from LREE/HREE $\sim$ 1 (i.e., a flat REE pattern) and a small Eu anomaly in the mantle melilite to a LREE/HREE ratio $>$ 10 and a large Eu anomaly in melilite from the core of the inclusion. These features are typical of melilite in Type B1 CAIs (e.g., MacPherson et al., 1989; Davis et al., 1992). On the other hand, large enrichments of REEs near spinel inclusions (e.g., open squares in Fig. 3a) have not been previously described. REE abundances are also highly variable in high-Ca pyroxene (Table 3; Fig. 3b). All fassaites are characterized by negative Eu anomalies and HREE-enriched patterns with 8–150 $\times$ ch La and 35–300 $\times$ ch Er. Note that the REE patterns from the core of the clinopyroxene with a patchy distribution of TiO_2 and from the enclosing overgrowth are virtually identical. REE abundances in fassaite from 3655A are within the range of values observed by Kuehner et al. (1989b) and Simon et al. (1991) in fassaite from other Type B1 CAIs. As in melilite, abundances of the REEs are enhanced in the vicinity of spinel inclusions. Perovskite (Table 4; Fig. 3c) contains high but variable levels of REEs (La 100–550 $\times$ ch) with a relatively flat pattern for the light to middle REEs, a negative Eu anomaly, and lower HREE abundances. Plagioclase (Table 4; Fig. 3d) is LREE-enriched with $\sim$10 $\times$ ch La and 1 $\times$ ch Yb and has a large positive Eu anomaly (60–70 $\times$ ch).

4.2. Barium, Strontium, and Hafnium

Measured Ba concentrations vary between 17 and 81 ppm in melilite, 110 and 112 ppm in plagioclase, 16 and 40 ppm in perovskite, and between 0.3 and 13 ppm in fassaite. The Ba concentrations increase with increasing Ak content in

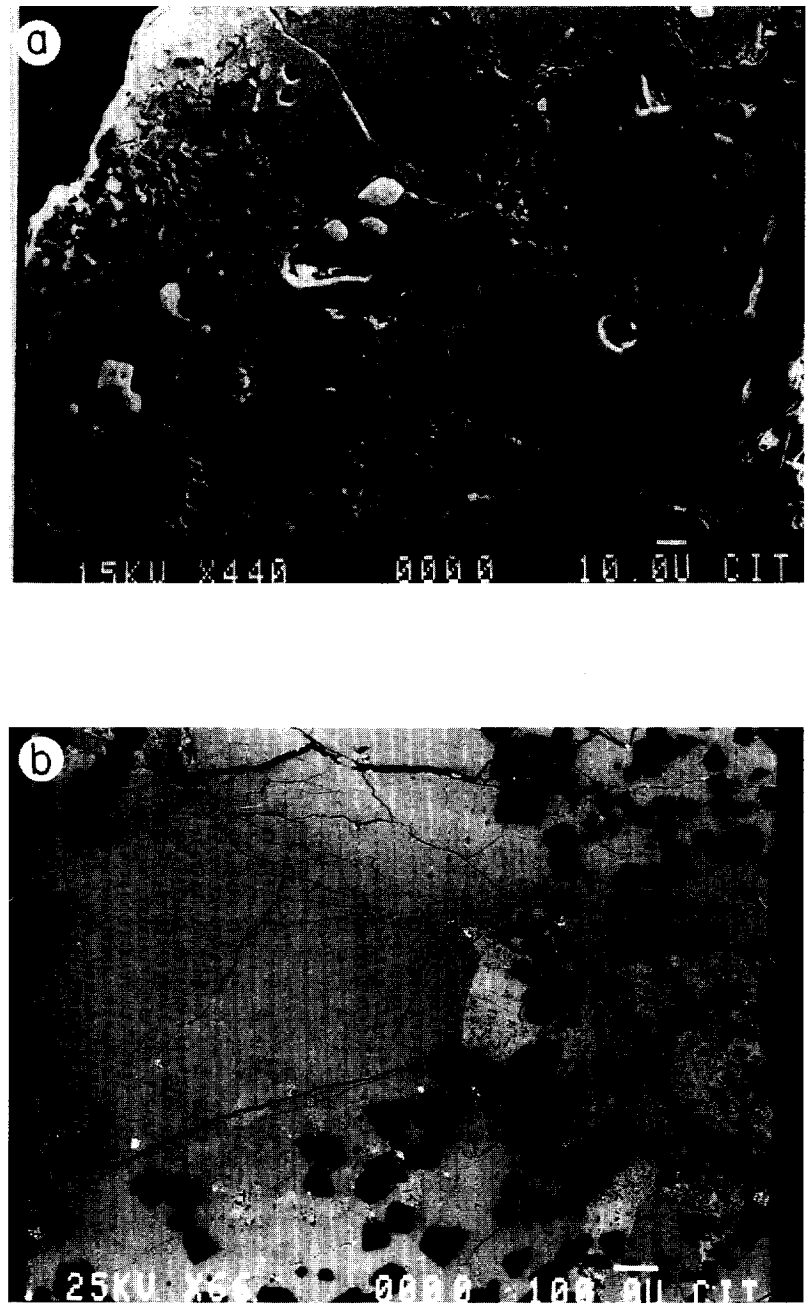

Fig. 2. (a) Backscattered electron image of perovskite grains (white) in mantle melilite (gray) of 3655A. Part of a spinel palisade (dark gray) is visible along the right-hand edge of the photo. Note the rounded to sinuous shape of perovskite, the close association of perovskite with the spinel palisade, and the alignment of perovskite within the melilite. The scale bar is 10 μm. (b) Backscattered electron image of a patchy cored clinopyroxene from the core of 3655A. The black crystals are spinel and the mottled gray regions are altered melilite. Note the ion microprobe pits across the center of the image. The inflection point of the series of points corresponds to the boundary between two clinopyroxene crystals. Variation of gray intensity of clinopyroxene reflects variations of TiO_2 concentrations between 3 and 13% in the patchy core shown in the lower central region of the photo. The scale bar is 100 μm.

melilite and from the core to rim in plagioclase and pyroxene crystals. Strontium concentrations are 470–495 ppm in plagioclase and 202–395 ppm in perovskite. Concentrations in melilite range from ~160 ppm Sr in the outer part of the melilite mantle (Ak10) to 314 ppm in the core of the inclusion (Ak65). Hafnium concentrations are 6 to 26 ppm in perovskite, <0.05 to 0.3 ppm in melilite, and below the detection limit of 50 ppb in plagioclase. Abundances of Hf and Sr were not measured in pyroxene.

4.3. Magnesium Isotopes

The Mg isotope compositions of primary and secondary silicate and oxide minerals located throughout 3655A were

Table 2. REEs, barium, hafnium, and strontium abundances in melilite in 3655A*.

Point[@]	X_{Ak}	Ba	La	Ce	Nd	Sm	Eu	Dy	Er	Sr	Hf
1-1	0.24	24	4.1	10.1	7.5	2.6	1.3	4.6	3.3		
1-2	0.27	22	3.8	8.5	6.3	2.1	1.4	2.5	1.6		
1-3	0.26	25	3.6	8.2	5.8	1.8	1.5	2.3	1.5		
1-4	0.24	30	4.2	9.0	6.2	2.0	1.4	2.7	1.9		
1-5	0.32	39	5.3	11.6	7.4	2.2	1.6	3.4	2.5		
1-6	0.37	41	4.3	8.5	5.2	1.4	1.7	1.9	1.4		
1-7	0.43	42	5.7	11.7	6.5	1.8	1.7	2.3	1.5		
1-8	0.41	37	4.7	9.7	5.5	1.5	1.4	1.4	0.80		
1-9	0.55	81	3.7	7.4	4.2	1.2	2.6	1.5	1.1		
1-10	0.62	57	2.2	4.3	2.5	0.86	1.4	1.2	0.95		
1-11	0.42	33	3.6	7.1	4.0	1.1	1.5	1.6	0.86		
1-12	0.40	27	4.3	8.3	4.9	1.2	1.2	1.3	0.68		
1-13	0.45	38	3.8	7.5	4.3	1.1	0.99	1.5	1.1		
1-14	0.55	31	1.3	2.3	1.4	0.37	0.98	0.19	0.11		
1-15	0.59	33	0.91	1.8	0.93	0.21	0.99	0.13	0.10		
1-16[†]	0.64	59	8.8	15.9	7.2	1.6	1.4	1.9	1.2		
1-20[†]	0.55	58	11.2	23.6	13.1	3.5	2.2	5.8	3.5		
1-21	0.57	33	1.1	2.0	1.1	0.27	1.0	0.22	0.09		
1-22	0.60	45	1.8	3.0	1.6	0.27	1.1	0.18	0.11		
2-1[‡]	0.25	17	1.7	3.9	3.6	1.2	1.2	1.8	1.0	153	0.3
2-2	0.09	24	2.4	5.7	4.8	1.8	1.2	2.9	1.6	166	0.01
2-3	0.03	24	3.3	7.9	6.7	2.3	1.3	3.5	2.2	164	0.3
2-4	0.04	26	1.2	2.7	1.9	0.82	0.98	1.2	0.69	173	0.10
2-5	0.10	17	3.2	7.9	6.9	2.2	1.2	2.6	1.4	160	0.08
2-6	0.09	22	1.7	3.9	3.7	1.2	1.2	1.9	1.0	158	0.04
2-7[‡]	0.05	28	1.2	2.6	1.8	0.81	0.98	1.2	0.69	159	0.2
3-1	n.m.	55	5.8	10.2	5.5	1.6	2.8	2.0	1.2	n.m.	n.m.
4-1[‡]	0.65	53	0.20	0.28	0.14	0.022	0.14	0.008	—	314	0.04

* All trace element abundances are in ppm. Typical 2σ uncertainties based on counting statistics for standards and unknowns are Sr 5%; Ba, La, Ce ~8%; Nd, Eu ~15%; Sm 20%; Dy, Er 40%; Hf 45%. Mole fraction of akermanite calculated from cations of Mg and Al. Strontium and hafnium were not measured in Traverse 1.

[@] Each analysis is designated by a traverse or region number following by the analysis point within the series of analyses. 1 denotes two traverses that extend across the melilite mantle. Ion microprobe pits from these analyses can be seen in Fig. 1. 2 denotes melilite points near the rim of the inclusion and adjacent to the small spinel palisade in Fig. 1. 3-1 is a small grain included within the core clinopyroxene with patchy TiO_2 distribution. 4-1 is a melilite in the core of 3655A.

[†] Melilite adjacent to spinel inclusions.

[‡] Pr and Gd were measured in 2-1 (0.58 ppm and 1.3 ppm), 2-7 (0.41 ppm and 1.0 ppm), and 4-1 (0.03 ppm and 0.014 ppm). Uncertainties for Pr and Gd are ~10% and 40%, respectively.

n.m. not measured.

— denotes below detection limit.

determined (Tables 5–8) with special attention devoted to high precision measurements of the intrinsic isotope fractionation (F_{Mg}). Differences in F_{Mg} among coexisting phases may occur if relict phases are preserved and the magnitude of Mg isotope heterogeneity in these crystals can be a sensitive indicator of CAI thermal history (Sheng et al., 1992). In subsequent sections, we will present both the standard error on the mean and the sample standard deviation to facilitate comparisons. The standard error on the mean assumes that there is a single true value for F_{Mg} for a mineral. This is unlikely to be true for spinel, which has F_{Mg} values ranging from 1.4 to 4.9‰/amu and a large standard deviation. Fassaite is much more homogeneous, and the calculation of a standard error on the mean is justifiable. The uncertainty given for all mean values is twice the standard error on the mean. The standard error on the mean is best considered an estimate of the uncertainty of a bulk F_{Mg} value for a mineral.

All of the phases in 3655A except grossular and monticellite, alteration products of melilite, are enriched in the heavier Mg isotopes, but the distribution of F_{Mg} values is not uniform. Fassaite displays a very homogeneous array of F_{Mg} values (Table 5; Fig. 4a). The mean of sixteen analyses is 3.6 ± 0.3‰/amu, and no individual analysis lies more than two standard deviations away from the mean. The mean F_{Mg} of twenty-four spinel analyses, 3.3 ± 0.4‰/amu, is indistinguishable from the fassaite value, but the spinels display much greater scatter with a $2\sigma_{sample}$ of 1.7‰, and F_{Mg} values ranging from 1.4 to 4.9‰/amu (Table 6; Fig. 4b). In addition, spinels from the small palisade near the rim (mean F_{Mg} = 4.4 ± 0.6‰/amu and a $2\sigma_{sample}$ of 0.9‰,) exhibit greater enrichment of the heavier Mg isotopes than do spinels from the large palisade (mean F_{Mg} = 3.1 ± 0.5‰/amu and a $2\sigma_{sample}$ of 1.1‰,). There is a greater range in F_{Mg} of spinel in the outer region of the melilite mantle when compared to spinel in the core of the inclusion. Melilites in 3655A exhibit relatively uniform Mg isotope fractionation but with a distinctly more positive mean F_{Mg} (5.3 ± 0.5‰/amu; thirty-two analyses and a $2\sigma_{sample}$ of 1.6‰,) than either fassaite or spinel (Table 7; Fig. 4c). In an effort to understand better the nature of this difference, we determined F_{Mg} values in fassaite and melilite at four fassaite-melilite contacts. In every case, melilite exhibits a larger F_{Mg} value than does the adjacent fassaite; the mean difference in F_{Mg} is 1.6 ± 0.2‰/amu (Fig. 4d). Hibonite in the rim exhibits

Table 3. REEs and barium abundances in clinopyroxene in 3655A*.

Point[@]	X_{TP}[†]	X_{Di}[‡]	Ba	La	Ce	Nd	Sm	Eu	Dy	Er
1-1	0.25	0.52	13	3.2	12.0	13.4	5.6	0.33	11.1	8.2
1-2	0.23	0.52	0.5	2.4	8.9	10.3	4.4	0.20	9.1	6.3
1-3	0.24	0.51	1.5	2.1	8.3	9.4	4.0	0.19	8.3	6.0
1-4	0.34	0.47	1.1	2.2	8.1	8.8	3.8	0.17	7.9	5.4
1-5	0.23	0.51	0.3	2.4	9.4	10.9	4.8	0.22	9.5	6.5
1-6	0.23	0.51	0.3	2.0	8.4	10.4	4.4	0.18	8.8	6.5
1-7	0.16	0.50	0.3	3.7	14.5	17.0	7.2	0.26	14.6	10.2
1-8	0.36	0.46	0.9	2.8	10.0	10.5	4.0	0.22	8.8	6.2
1-9	0.38	0.43	1.5	1.8	7.1	8.6	3.7	0.18	7.9	5.4
1-10	0.32	0.47	0.4	1.7	7.2	8.8	3.9	0.18	8.1	5.5
1-11	0.24	0.53	0.3	2.0	8.3	9.9	4.4	0.18	9.1	6.6
1-12	0.18	0.55	0.4	2.3	9.4	11.1	4.8	0.18	10.1	7.4
1-13	0.15	0.55	0.3	2.7	11.2	13.7	5.7	0.23	12.3	9.1
1-14	0.12	0.58	3.2	3.2	12.3	14.9	6.4	0.30	13.2	10.4
1-15	0.11	0.58	0.3	3.1	12.6	14.5	6.4	0.28	13.7	10.1
1-16	0.10	0.60	0.3	3.3	13.0	15.9	6.7	0.26	14.3	10.9
1-17	0.08	0.57	5.5	35.8	115.0	91.5	29.1	0.65	58.6	49.7
2-1	0.35	0.44	1.0	2.3	8.2	9.3	3.9	0.19	8.2	5.9
2-2	0.28	0.49	0.3	1.8	7.4	9.6	4.0	0.19	8.4	6.2
2-3	0.24	0.54	0.4	2.0	8.3	10.1	4.4	0.19	9.1	6.8
2-4	0.20	0.53	0.3	2.1	8.8	10.9	4.6	0.19	10.3	7.2
2-5	0.17	0.58	1.5	2.5	10.1	12.4	5.3	0.22	11.5	8.8
3-1	0.29	0.51	0.3	2.0	8.1	9.3	4.0	0.18	8.0	5.6
3-2	0.35	0.45	0.4	1.6	6.3	7.4	3.2	0.14	7.2	5.7
3-3	0.32	0.46	1.2	4.3	13.4	11.6	4.6	0.18	9.5	6.9
3-4	0.31	0.46	0.5	2.1	8.6	9.4	4.0	0.16	8.6	6.6
3-5	0.32	0.48	0.5	2.0	8.4	9.8	4.0	0.16	8.3	6.1
3-6	0.37	0.43	0.4	1.6	6.9	8.5	3.7	0.18	7.6	5.6
3-7	0.28	0.50	3.4	2.4	9.8	12.0	4.9	0.19	10.4	7.7
3-8	0.21	0.51	0.4	3.5	14.7	17.1	7.3	0.25	14.8	10.8
3-9	0.13	0.53	11	5.5	18.8	19.3	7.8	0.98	16.2	12.9

* All trace elements abundances in ppm. Typical 2σ uncertainties based on counting statistics for standards and unknowns are Ba 20%; La, Ce, Nd 8%; Sm 15%; Eu 25%; and Dy, Er 8%.

[†] X_{TP} is the calculated mole fraction of Ti pyroxene. $X_{TP} = X_{T3P} + X_{T4P}$, where X_{T3P} and X_{T4P} are the respective mole fractions of Ti^{3+} and Ti^{4+} pyroxene calculated from major element compositions and stoichiometry. X_{T3P} for all analyses is <0.1 and $< 1/3$ of X_{TP}.

[‡] X_{Di} is calculated mole fraction of diopside. $X_{CaTs} = 1 - X_{Di} - X_{TP}$ where CaTs refers to the Ca-Tschermak's molecule $CaAl_2SiO_6$.

[@] Clinopyroxenes 1 and 2 data refer to a traverse across two adjacent pyroxenes, one of which has patchy TiO_2 distribution. 1-1 through 1-9 are from the patchy core of the crystal, 1-10 through 1-16 from overgrowth pyroxene with smoothly decreasing TiO_2 that surrounds the core. 2-1 through 2-5 are from the adjacent crystal. Point 1-17 is on the boundary between the two crystals. 3-1 through 3-3 and 3-4 through 3-7 are traverse toward spinel inclusions within clinopyroxene in the inclusion core. 3-7 through 3-9 are from a single pyroxene grain near the boundary of the core and melilite mantle.

the greatest Mg isotope fractionation (mean F_{Mg} = 8.4 ± 2.0‰/amu and a $2\sigma_{sample}$ of 2.1‰) while grossular (−0.2 ± 2.4‰/amu) and monticellite (−1.9 ± 1.6‰/amu) show no evidence of mass-dependent fractionation. These differences in mean F_{Mg} values among the various phases are clearly visible in Fig. 4e.

Table 4. REEs, barium, hafnium, and strontium abundances in ppm of perovskite and plagioclase in 3655A.

	Ba	La	Ce	Pr	Nd	Sm	Eu	Gd	Tb	Dy	Er	Yb	Sr	Hf
Perovskite[†]														
*1	40	25	70	11	644	15	2.0	25	4.3	27	18	11	202	6
2	23	107	330	52	258	83	3.3	123	18.0	91	44	28	389	26
*3	16	130	386	58	297	97	2.8	162	29.0	152	79	26	395	20
Plagioclase[‡]														
core	110	2.1	3.9	0.38	1.6	0.31	3.3	0.24	—	0.22	0.18	0.15	470	b.d.
rim	112	2.1	3.9	0.41	1.5	0.35	3.4	0.33	—	0.21	0.19	0.17	495	b.d.

[†] Perovskite analysis 1 is from a grain attached to the small spinel palisade in region E of Fig. 1 and grains 2 and 3 are isolated crystals included in melilite ~50 and ~150 μm, respectively, from the edge of the inclusion.

* Data for perovskites 1 and 3 were corrected respectively for 5% and 3% overlap of the ion microprobe beam onto melilite. These corrections are minor for all elements with the exception of Ba and Sr. Typical uncertainties for perovskite based on counting statistics for standards and unknowns are: Ba 6%; La, Ce, Pr, Nd, Sm, Dy, Er < 2%; Tb, Yb, Sr, Hf ~4%; Eu, Gd ~6%.

[‡] For plagioclase typical 2σ uncertainties are: Sr 3%; Ba 4%; La, Ce 10%; Nd, Eu 15%; Pr, Sm ~20%; Dy, Er, Yb 40%. b.d. below detection limit of 50 ppb.

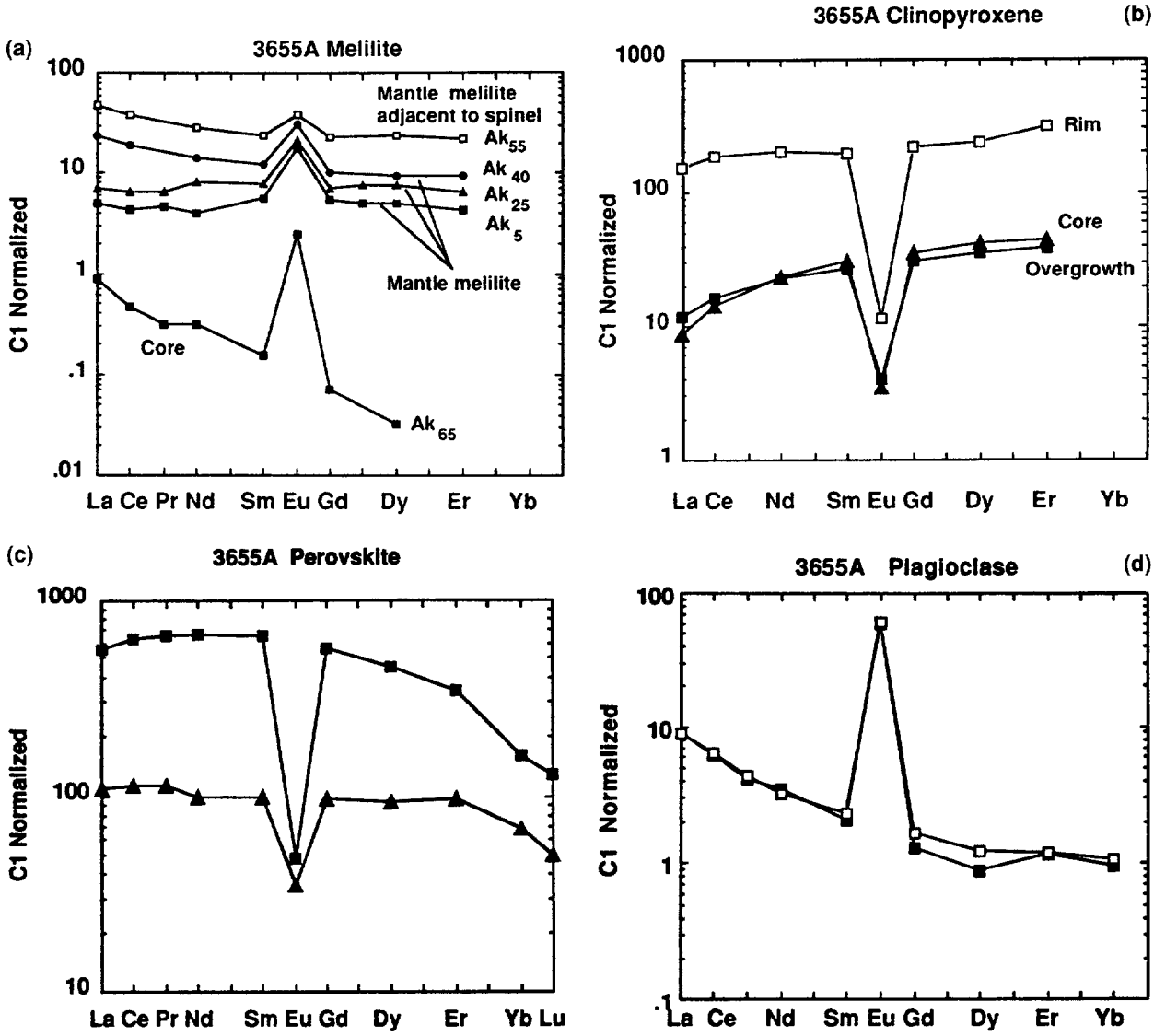

Fig. 3. Representative chondrite normalized REE patterns of phases in 3655A. Chondritic values are from Anders and Grevesse (1989). (a) Melilite from the mantle and core (filled symbols). Akermanite contents are indicated next to each pattern. A representative REE pattern of a melilite adjacent (10 μm) to a spinel is also shown (open squares). (b) Clinopyroxene crystal from the inclusion core. The pattern labeled core (triangles) is from the patchy TiO_2 core of the crystal, the pattern labeled overgrowth (filled squares) is from the smoothly zoned overgrowth region, and the rim pattern (open squares) is from the very edge of this crystal where it abuts against another clinopyroxene. (c) Perovskite ~150 μm from the rim of the inclusion (squares) and attached to the small spinel palisade (triangles) ~300 μm from the rim. (d) Plagioclase crystal from the core of 3655A. Analyses are from the rim (unfilled symbols) and core (filled symbols) of the crystal.

Excess ^{26}Mg is found in plagioclase, hibonite, and melilite and the measured $\delta^{26}Mg$ values in these phases are linearly correlated with the respective $^{27}Al/^{24}Mg$ ratios. On an ^{26}Al-^{26}Mg evolution diagram (Fig. 5a,b), these data define a linear array with a slope corresponding to $^{26}Mg^*/^{27}Al = (3.95 \pm 0.42) \times 10^{-5}$, a value similar to that measured in many Allende Type B1 CAIs (Hutcheon, 1982; Podosek et al., 1991). Data from seven of eight melilite crystals lie within two standard deviations of the line (Fig. 5b), suggesting that 3655A did not experience extensive metamorphic redistribution of $^{26}Mg^*$. Despite $^{27}Al/^{24}Mg$ ratios as high as 50, grossular located in the melilite-rich mantle shows no evidence of radiogenic $^{26}Mg^*$ ($^{26}Mg^*/^{27}Al < 1.5 \times 10^{-5}$).

5. THE DISTRIBUTION OF TRACE ELEMENTS IN 3655A

5.1. Melilite

Beckett et al. (1990) have shown that for a trivalent REEs, the equilibrium melilite/melt partition coefficient defined as $K_{mel,i} \equiv c_i^{mel}/c_i^{Liq}$, where c_i^j is the concentration of element i in phase j, depends on the major element chemistry of the melilite with $K_{mel,i}$ decreasing as akermanite content in-

Table 5. Magnesium isotope composition of fassaite in 3655A.

Distance (μm)[1]	F_{Mg} (‰/amu)[2]	δ^{26}Mg (‰)[2]
1300	4.4 ± 0.8	0.3 ± 0.7
1350	3.5 ± 0.8	−0.2 ± 1.4
1490	3.3 ± 0.8	−0.4 ± 1.8
1620	3.3 ± 0.7	1.7 ± 1.6
1700	3.8 ± 1.4	1.1 ± 1.4
1900	3.4 ± 1.2	1.7 ± 1.4
2500	3.9 ± 0.9	0.4 ± 1.6
2650	4.3 ± 0.7	−1.2 ± 2.3
2750	3.9 ± 0.9	0.7 ± 1.5
2850	4.4 ± 0.7	0.8 ± 1.9
3000	3.1 ± 0.8	1.8 ± 1.5
3250	3.0 ± 0.8	−0.6 ± 1.4
3700	3.3 ± 0.7	2.3 ± 2.2
3800	3.3 ± 0.7	1.3 ± 1.8
4100	3.4 ± 1.2	1.4 ± 2.6
4400	3.8 ± 1.4	−0.6 ± 2.2

[1] Radial distance inward from the rim of the inclusion.
[2] Uncertainties are two standard deviations of the mean.

creases. $K_{mel,La}$, for example, decreased from 0.3 at Ak25 to 0.07 at Ak75 in their experiments. This behavior produces the unusual circumstance in which the concentration of an incompatible trace element ($K_{mel,i} < 1$) in melilite actually decreases as crystallization proceeds. Since spinel and melilite crystallize for ~200°C before the appearance of pyroxene and/or plagioclase (Stolper and Paque, 1986) and spinel/melt partition coefficients for trace elements are extremely small except for the transition elements (Nagasawa et al., 1980), the distribution of trace elements in early crystallizing melilite from 3655A should be controlled by melilite/melt partitioning provided the melt composition was initially homogeneous. There are small inclusions of clinopyroxene in mantle melilite. However, the small volume fraction and low pyroxene/melt partition coefficients for the REEs, typically ~0.1 for La, ~0.6 for Yb (Kuehner et al., 1989a; Simon et al., 1991), and <0.01 for Ba (Hart and Brooks, 1977), imply a negligible effect on the distribution of REEs and Ba between melilite and liquid.

Figure 6a shows the concentration of La plotted against the akermanite content of melilite from the mantle of 3655A. Two points with anomalously high REEs in Fig. 6a are from melilite adjacent to included spinel; these data are discussed

Table 6. Magnesium isotope composition of spinel in 3655A.

Distance (μm)[1]	Location	F_{Mg} (‰/amu)[2]	δ^{26} Mg (‰)
100	Rim	2.7 ± 1.0	0.0 ± 1.7
125	Rim	3.4 ± 0.9	1.3 ± 1.5
140	Rim	2.2 ± 1.2	1.2 ± 2.0
150	Small Palisade	4.8 ± 0.8	1.6 ± 1.1
180	Small Palisade	4.2 ± 1.2	2.7 ± 2.1
270	Small Palisade	3.9 ± 1.0	0.1 ± 1.6
450	Mantle	3.1 ± 1.0	0.4 ± 1.7
500	Mantle	3.2 ± 1.3	−0.5 ± 2.1
580	Mantle	1.4 ± 1.1	1.4 ± 1.1
850	Mantle	3.1 ± 1.0	1.8 ± 1.5
1475	Large Palisade	2.2 ± 1.4	1.5 ± 2.0
1500	Large Palisade	3.5 ± 1.2	0.8 ± 1.6
1520	Large Palisade	3.3 ± 1.3	1.7 ± 1.8
1580	Large Palisade	2.9 ± 0.9	2.3 ± 2.0
1620	Large Palisade	3.9 ± 1.4	0.6 ± 1.6
3600	Interior	2.3 ± 1.5	−2.1 ± 2.5
3900	Interior	4.9 ± 1.4	−0.7 ± 2.4
4100	Interior	2.9 ± 1.3	1.0 ± 2.2
4400	Interior	3.2 ± 1.2	−0.4 ± 2.4
4500	Interior	2.3 ± 1.3	2.4 ± 2.0
4600	Interior	4.7 ± 1.4	0.5 ± 2.0
4750	Interior	3.7 ± 1.7	−2.0 ± 2.2
4850	Interior	3.4 ± 0.8	0.7 ± 1.4
4900	Interior	3.3 ± 0.7	1.7 ± 1.6

[1] Radial distance inward from the rim of the inclusion.
[2] Uncertainties are two standard deviations of the mean.

Table 7. Magnesium isotope composition in melilite in 3655A.

Distance (μm)[1]	F_{Mg} (‰/amu)[2]	δ^{26}Mg (‰)[2]	^{27}Al/^{24}Mg
100	6.0 ± 2.3	4.1 ± 3.0	11
180	7.2 ± 1.8	−2.3 ± 2.6	13
200	6.1 ± 2.3	2.7 ± 2.1	7.5
280	4.8 ± 2.1	6.9 ± 3.3	22
400	6.4 ± 1.7	5.1 ± 2.4	21
700	4.7 ± 1.7	3.4 ± 2.5	14
1020	4.4 ± 1.1	1.0 ± 1.6	2.0
1150	4.3 ± 1.1	0.7 ± 1.6	1.7
1250	5.5 ± 1.0	1.4 ± 1.6	1.5
1300	5.9 ± 1.0	0.6 ± 1.5	2.0
1550	6.1 ± 1.4	1.1 ± 1.7	3.0
1600	5.4 ± 1.6	5.3 ± 2.2	8.0
2200	4.2 ± 1.5	0.1 ± 1.6	4.0
2550	5.5 ± 1.0	1.3 ± 2.4	2.6
2700	5.9 ± 0.9	0.3 ± 1.7	1.4
2750	4.9 ± 1.1	1.7 ± 2.6	2.7
2800	5.0 ± 1.0	0.7 ± 1.7	1.5
2900	6.0 ± 1.5	1.2 ± 1.9	5.0
2950	5.6 ± 1.2	1.4 ± 1.8	1.5
3050	6.1 ± 1.5	1.9 ± 2.3	3.3
3100	6.2 ± 1.2	0.3 ± 1.9	3.4
3200	4.5 ± 1.8	−0.6 ± 2.9	1.5
3400	4.5 ± 1.6	2.2 ± 3.0	3.0
3700	4.9 ± 1.0	3.0 ± 2.4	2.7
3850	5.0 ± 1.0	0.7 ± 2.5	2.3

[1] Radial distance inward from the rim of the inclusion.
[2] Uncertainties are two standard deviations of the mean.

Table 8. Magnesium isotope composition of anorthite, hibonite, grossular and monticellite in Allende 3655A.[1]

Sample	F_{Mg} (‰/amu)[2]	δ^{26}Mg (‰)[3]	^{27}Al/^{24}Mg[4]
Anorthite 1	−0.2 ± 2.5	60.9 ± 4.2	220 ± 15
Anorthite 2	−2.8 ± 2.4	51.8 ± 7.6	185 ± 10
Anorthite 3	−3.4 ± 3.0	99.2 ± 8.5	322 ± 30
Anorthite 4	−0.9 ± 2.5	102 ± 3.4	380 ± 18
Hibonite 1	7.4 ± 3.5	13.9 ± 3.4	40 ± 3
Hibonite 2	8.8 ± 2.5	5.3 ± 3.5	25 ± 3
Grossular	−0.2 ± 2.6	1.5 ± 2.6	50 ± 4
Monticellite	−1.9 ± 1.6	0.4 ± 2.8	0.01

[1] Uncertainties are expressed as two standard deviations of the mean.
[2] Permil deviation from the ^{25}Mg/^{24}Mg ratio measured in a mineralogically similar standard.
[3] Permil deviation from ^{26}Mg/^{25}Mg = 0.13955 after normalizing to ^{25}Mg/^{24}Mg = 0.12663 using a power law to correct for mass fractionation.
[4] Calculated from secondary ion intensity ratios, as described in the text.

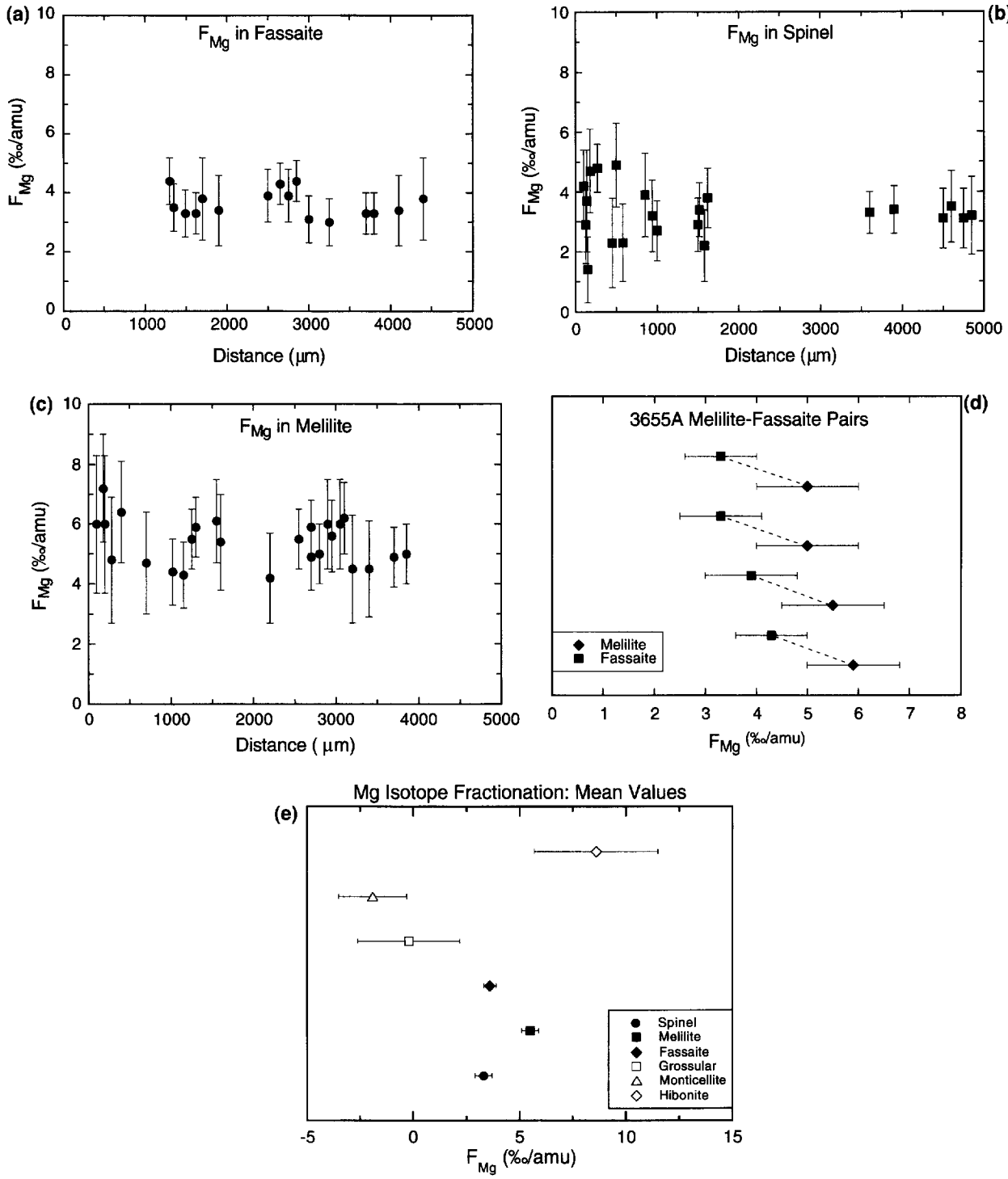

Fig. 4. Mass-dependent isotope fractionation of Mg in 3655A. (a-c) Mg isotope compositions of fassaite, spinel, and melilite, respectively, shown as a function of distance along a traverse radially inward from the rim of the inclusion. (d) The distribution of F_{Mg} values for four melilite-fassaite pairs; the dashed lines connect data for adjoining grains. In each case, F_{Mg} is lower in fassaite than in the adjacent melilite. (e) Mean F_{Mg} values for primary (spinel, fassaite, melilite, and hibonite) and secondary (grossular and monticellite) phases in 3655A. The error bars are $\pm 2\sigma_{mean}$.

below. Also shown in Fig. 6a is a calculated La concentration trajectory for equilibrium fractional crystallization of melilite. This curve is based on the experimental partition coefficient data and semi-empirical expression relating $K_{mel,i}$ and X_{Ak} of Beckett et al. (1990), the assumption of a homogeneous initial liquid with 20 × ch REEs (e.g., Mason and Taylor, 1982), and that $F = 0.521 + 0.019/X_{Ak}$ where F is the fraction of melt remaining. Coefficients in the expression

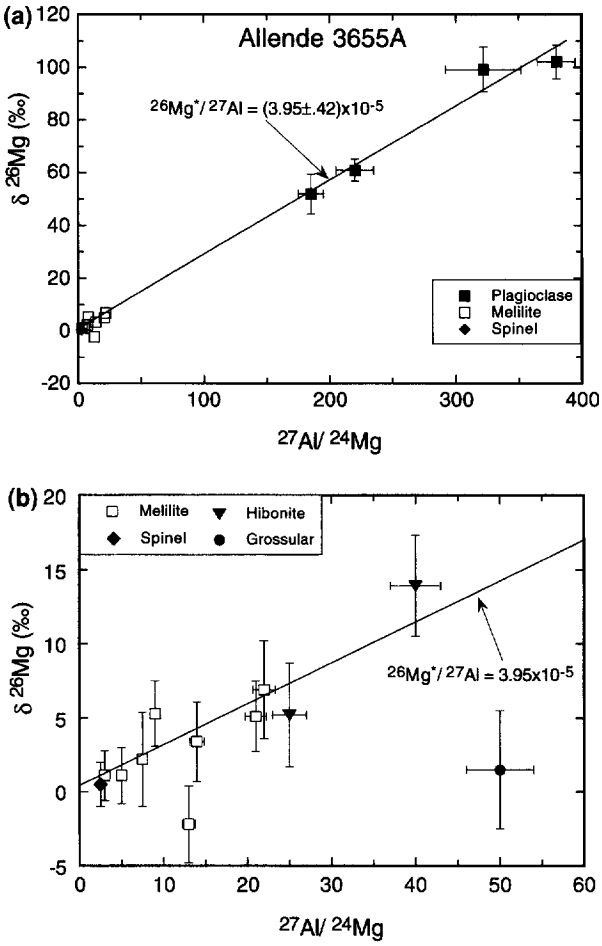

Fig. 5. ^{26}Al-^{26}Mg isotope systematics for 3655A. (a) ^{26}Al-^{26}Mg evolution diagram for anorthite, melilite, and spinel. The data define a correlation line with a best-fit slope similar to, but slightly lower than, the canonical early Solar System $(^{26}Al/^{27}Al)_0$ ratio of 5×10^{-5}. (b) Expanded view of the region of Fig. 5a with $0 < ^{27}Al/^{24}Mg < 60$, showing data for spinel (mean value), melilite, grossular, and hibonite; data for melilite with $^{27}Al/^{24}Mg < 5$ are not shown. The data for seven of eight melilites lie within the analytical uncertainty of the best-fit line from Fig. 5a. The data for grossular show no evidence of excess $^{26}Mg^*$. All error bars are $\pm 2\sigma_{mean}$.

for F were obtained by assuming that melilite first crystallized with $X_{Ak} = 0.05$ preceded by crystallization of 10 wt% spinel and that $X_{Ak} = 0.65$ and $F = 0.55$ at the core-mantle interface. The selected coefficients are not well constrained because neither the thin section, which samples only a portion of the inclusion, nor the bulk analysis of Mason and Taylor (1982), which almost certainly reflects more core than mantle material, are representative. The calculated values of F are, however, typical of Type B1 inclusions (Beckett, 1986; Beckett et al., 1990; Simon et al., 1994). Measured La concentrations in 3655A melilite rise from 1 to 3 ppm in Ak5-Ak10 melilite to a maximum of ~6 ppm at Ak40 and then decrease to <0.1 ppm in the most akermanitic melilite (Ak65). The concave downward profile in La concentration contrasts sharply with the predicted trend. Variations in the La concentration in melilite at any given Ak content, ±20–50%, are also far larger than variations observed, <±5%, in the experiments of Beckett et al. (1990), suggesting that the La concentration in the 3655A melt at the melilite/melt interface was heterogeneous. The extreme variations at very high X_{Ak} may reflect crystallization of additional phases, but variations at lower X_{Ak} values cannot be explained in this way. Figure 6b shows that the concentration of Dy, like that of La, increases in 3655A melilite until ~Ak30, decreases slowly until Ak40, and then drops precipitously at higher X_{Ak}; this rapid drop is apparent in all four Type B1 inclusions. Again, the dependence of Dy content on X_{Ak} is the opposite of that expected for equilibrium fractional crystallization. Another important observation is that the concentrations of REEs in early crystallizing melilite are much lower than expected. Based on the partitioning experiments of Beckett et al. (1990) and Kuehner et al. (1989a), $K_{mel,La} \sim 1.8$ and $K_{mel,Dy} \sim 0.9$ for Ak5 melilite. Thus, for melt concentrations of 20 × ch, a typical bulk enrichment for a Type B1 inclusion, the first melilite to crystallize should have La ~ 8 ppm and Dy ~ 4 ppm, even higher if significant amounts of spinel crystallized first. Observed concentrations in Ak5 melilite from 3655A are generally much lower, 1–3 ppm for La and 1–4 ppm for Dy. Note that the discrepancy between predicted and observed abundances is greater for the LREEs. Lanthanum is too low by a factor of 3–8 vs. a factor of 1–4 for Dy. This discrepancy is reflected in the LREE/HREE ratios. In the experiments of Beckett et al. (1990), LREE/HREE ratios in melilite remain approximately equal to the ratio in the starting material, whereas the measured La/Dy and other LREE/HREE ratios increase substantially during crystallization of 3655A (Fig. 6c), even during the interval when pyroxene is not a crystallizing phase.

In contrast to the trivalent REEs, the concentration of Eu, a divalent cation at low oxygen fugacities, increases monotonically until plagioclase begins crystallizing at high X_{Ak}. Kuehner et al. (1989a) have shown experimentally that the partition coefficient for Sr, a divalent cation often used as an analog for Eu^{2+}, is less than, but close to, 1.0 for low X_{Ak} melilite and relatively independent of melilite composition. If Eu^{2+} behaves like Sr, then the slight increase of Eu with increasing X_{Ak} observed in 3655A melilite (Fig. 6d), is just the behavior predicted from experimental studies. Moreover, the concentration of Eu in the earliest crystallized melilite, ~1 ppm, is identical to the predicted value. Depletion of the melt in Eu, due to $K_{plag,Eu} > 1$, is reflected in the decrease in Eu in melilite for $X_{Ak} > 0.5$.

Barium is highly incompatible in melilite, with $K_{mel,Ba}$ in the range 0.05–0.09 (Beckett et al., 1990). Given a bulk concentration of 37 ppm in 3655A (Mason and Taylor, 1982), early crystallizing melilite should have less than 2 ppm Ba, and Ba concentrations should increase to ~3 ppm during the first 40% of crystallization. The measured Ba concentrations increase continuously as predicted (Fig. 6e), but the concentrations are 10 to 50 times higher than expected.

5.2. Pyroxene

Paque (1990) first noted the existence of clinopyroxenes in the interior of 3655A with patchy TiO_2 distributions and suggested that they might be relict. To examine this possibility, we analyzed specific points corresponding to high and

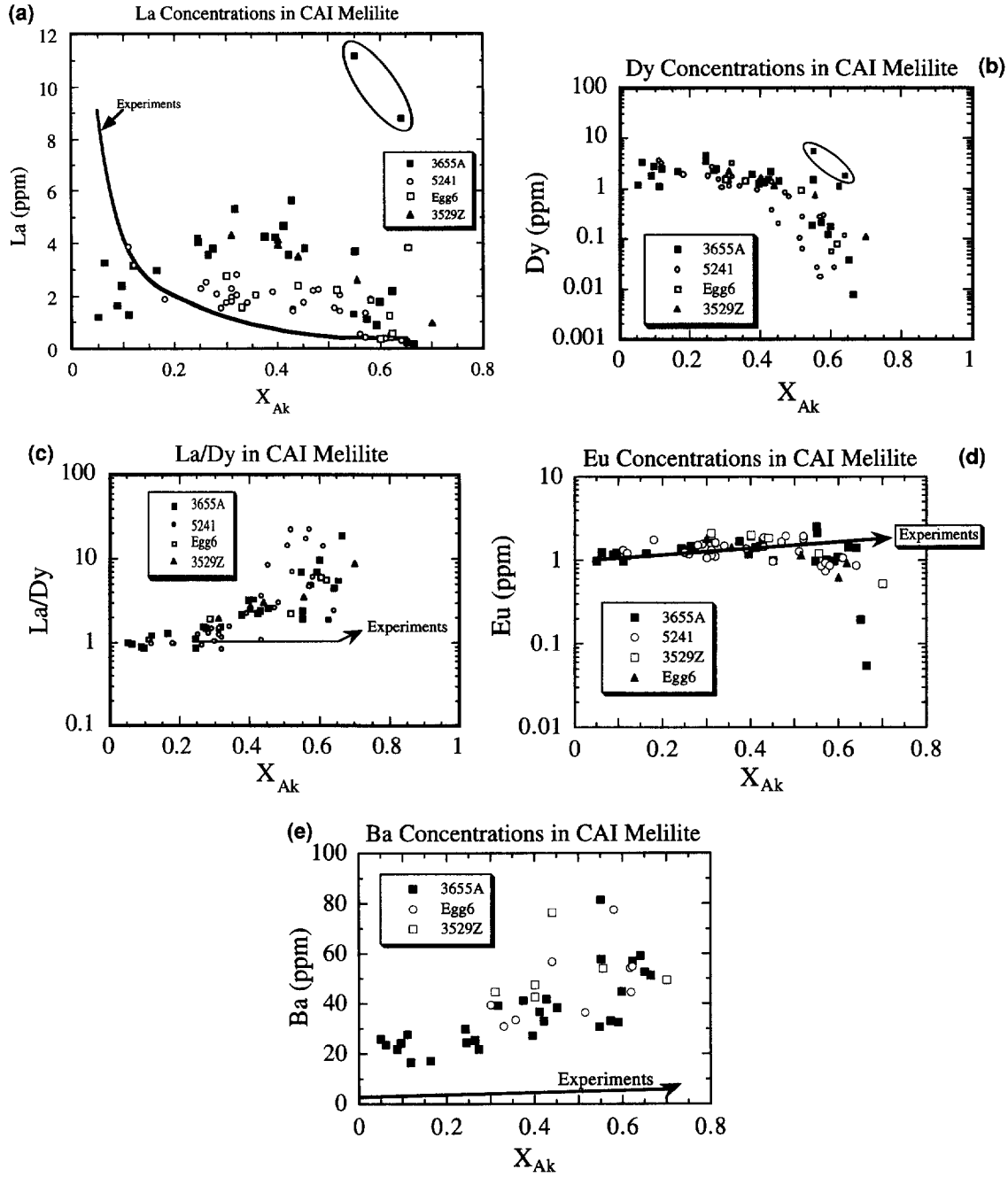

Fig. 6. Trace element distributions in 3655A mantle melilite as a function of akermanite content. (a) La. Also shown is a calculated curve for fractional crystallization based on experimental results from Beckett et al. (1990). The two anomalously high concentrations enclosed with an ellipse were analyses near spinel inclusions (see text). (b) Dy. Ellipse as in (a) also shown are melilite data on Type B1 inclusions 5241 (MacPherson et al., 1989), Egg 6, and 3529Z (Kennedy et al., 1988). (c) La/Dy. Additional data, as above, and a predicted curve based on the experimental data of Beckett et al. (1990). (d) Eu. Additional data as above. Curve calculated assuming fractional crystallization with $K_{mel,Eu} = 1$ and $K_{sp,Eu} = 0$. (e) Ba. Data for Egg 6 and 3529Z, as before. Regression curve from Beckett et al. (1990).

low TiO_2 in the patchy core of one pyroxene and measured trace element abundances along a traverse within the same grain. This traverse (Fig. 2b; see also Fig. 1 of Paque, 1990) extends from the center of the patchy region through the overgrowth zone to the edge of the crystal and into an adjacent clinopyroxene. Lanthanum and Dy concentrations (Fig. 7) increase as crystallization proceeds in the overgrowth on the patchy core, and there is no discontinuity across the boundary between the patchy core and overgrowth regions. The patchy core and overgrowth have essentially the same trace element concentrations (see also Fig. 3b), and neither the REE data nor the Mg-isotope compositions provide any

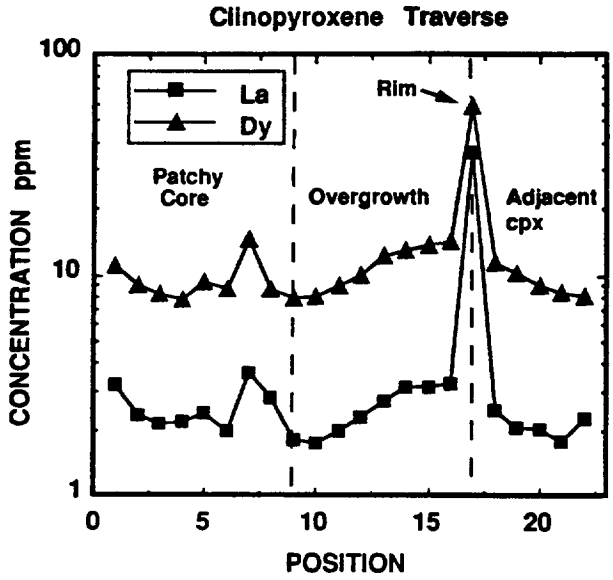

Fig. 7. Lanthanum and Dy concentrations along the traverse shown in Fig. 2b that crosses two grains of core clinopyroxene from 3655A. The distance between successive ion probe pits is ≈50 μm. The patchy core region contains points with 3 to 13% TiO_2. The overgrowth on this region and the adjacent grain have smoothly varying TiO_2. Enrichments in La and Dy occur at the boundary between the two grains (position 17) and adjacent to an included spinel in the patchy core (positions 7, 8).

evidence that these cores might be relict primary condensates. It is more likely that the unusual patchy zonation reflects some aspect of the thermal history of 3655A during the last melting event. It may, for example, be possible to produce a patchy Ti distribution by growing pyroxene that is incorporating a large number of spinels, as this may produce isolated melt pockets with different final Ti concentrations.

Two regions along the traverse within the core clinopyroxene (Fig. 7) have anomalously high trace element abundances. One occurs at the boundary between the two clinopyroxene grains (Fig. 2b). The REE pattern at this interface has a shape typical of clinopyroxene (Fig. 3c) but is highly enriched in REE (>100 × ch). We interpret the high concentrations to be the consequence of crystallization from the last fraction of the residual melt as suggested by Simon et al. (1991). The second unusually enriched point is from an analysis within 20 μm of a spinel grain. Dramatic enrichments of trace element concentrations are consistently observed within 20–60 μm of included spinel throughout 3655A, both for melilite and clinopyroxene. Figure 8 shows La concentrations from a series of analyses adjacent to spinel within melilite and clinopyroxene. In most instances, the host phase is enriched in trace elements within 60 μm of spinel, but the magnitude of the enhancement is variable, possibly reflecting differences in the orientation of a given traverse relative to the original direction of growth of the host phase. The difference in the level of enhancement between melilite and clinopyroxene may indicate differences in growth rates and/or interface kinetic processes, such as attachment and detachment, between melilite and clinopyroxene. Our data clearly identify these enrichments and point to the need for further study of this feature.

This discussion has revealed numerous discrepancies between the observed trace element abundances and distributions in 3655A and those expected for simple fractional crystallization models. Equilibrium fractional crystallization fails to explain either the abundances or the distributions of many trace elements in mantle melilite, the enrichment of trace elements adjacent to included spinel, and the occurrence of perovskite in the mantle. Measured REE and trace element concentrations, concentration ratios, dependence on X_{Ak}, and the variability of concentration at a given X_{Ak} all differ from what is expected. Nor are these observations unique to 3655A. In most instances, the Type B1 inclusions 3529Z, Egg 6, and 5241 show features similar to those observed in 3655A (Fig. 6a-e). In the following sections, we explore and, where possible, quantify the implications of these discrepancies for the thermal history and formation of 3655A and other Type B1 CAIs.

6. RELICT PHASES IN TYPE B1 CAIs

When the precursor to a Type B1 CAI undergoes partial melting at some maximum temperature, T_{max}, the solid phases that existed in the precursor will interact with the melt in one of three ways. First, a phase may be stable at T_{max} and dissolve into the melt at a rate defined by its solubility and the diffusivities of the major elements. Dissolution will cease when chemical equilibrium between the crystalline phase and the melt is reached. It is likely that spinel, the liquidus phase for 3655A, falls into this category. Second, a phase may be unstable in the melt at T_{max} but stable at some point on the binary joining compositions of the melt and solid phase. In this case, dissolution will occur at the rate given above for case #1, but bulk crystal-liquid equilibrium will never be achieved, and, given enough time, the phase will dissolve completely. In general, this behavior only oc-

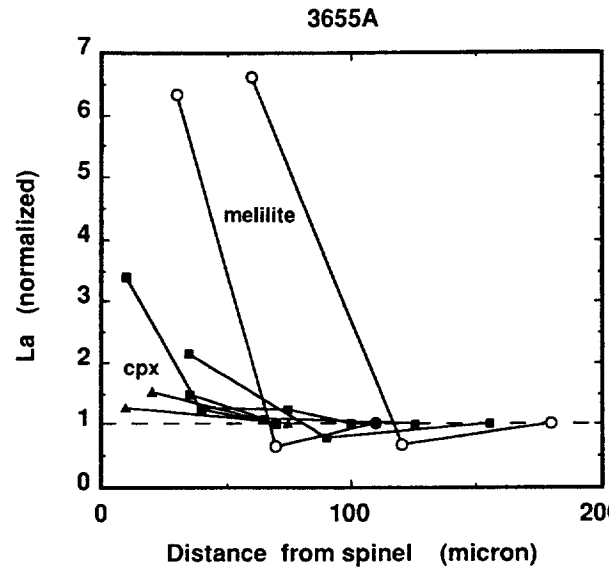

Fig. 8. Normalized La concentrations of melilite (open symbols) and clinopyroxene (closed symbols) adjacent to spinel in 3655A as a function of distance from the interface with spinel. Concentrations of La are normalized for each traverse to the concentration obtained from the analysis furthest from the included spinel.

curs for phases with melting points exceeding T_{max}. For 3655A, we may constrain T_{max} to be greater than the appearance temperature of melilite, ~1450°C, based on the bulk composition (Wark and Lovering, 1982) and the phase diagram of Stolper (1982), but less than 1574°C, the liquidus temperature according to the Berman (1983) model. For 1450°C < T_{max} < 1574°C, small amounts of refractory condensate phases, such as baddeleyite (T_{melt} = 2850°C), hibonite (T_{melt} = 1903°C), perovskite (T_{melt} = 1915°C), forsterite (T_{melt} = 1890°C), and grossite (T_{melt} = 1772°C) may be expected to fall into category #2. Anorthite (T_{melt} = 1557°C), enstatite (T_{melt} = 1559°C), gehlenitic melilite (T_{melt} = 1550°C for Ak5), and nepheline (actually carnegeite at the melting point of 1526°C) may also fall into this category, depending on T_{max}. The third type of interaction with the melt arises when a phase is completely unstable at T_{max}. The phase then melts outright, and homogenization is controlled strictly by diffusion in the melt. Fassaite ($T_{melt} \leq$ 1400°C), akermanitic melilite (T_{melt} = 1390°C for Ak65), and albite (T_{melt} = 1118°C) fall into this category.

6.1. The Effect of Relict Phase Composition on Trace Element Distributions

The dissolution of minerals strongly enriched in trace elements relative to the melt may noticeably perturb the trace element concentrations and zoning patterns of crystallizing phases. Perovskite, which readily incorporates large amounts of REEs and Nb (Clark, 1984; Fahey et al., 1987), and hibonite, which is sometimes highly enriched in REE, Zr, and Sc (Hinton et al., 1988; Ireland et al., 1988), are possible candidates for such a process. Upon dissolution, either of these phases could progressively enrich the melt in trace elements so that melilite crystallized during or after this time would exhibit an aberrant trace element zoning pattern relative to expectations based on equilibrium fractional crystallization. Perovskite is present in the outer portion of 3655A. It is unlikely to be a near-liquidus phase in melts generated from Type B1 CAIs (Stolper, 1982; Stolper and Paque, 1986) and has a rounded morphology consistent with partial dissolution. Moreover, the dissolution of perovskite with high LREE/HREEs relative to the coexisting melt will produce a melt with progressively increasing LREE/HREEs, and this will be reflected in the REE abundances of the melilite. The LREE/HREE ratio measured in 3655A melilites show this characteristic (Fig. 6c). We therefore argue that perovskite was dissolving during the initial stages of melilite crystallization.

Hibonite occurs only in a few small remnants of the Wark-Lovering rim of 3655A. However, the absence of this phase does not guarantee that there was no precursor hibonite that underwent dissolution during the earliest stages of crystallization. Blades of hibonite would have greater surface area than more equant perovskite, and this could result in enhanced dissolution rates. Hibonite that forms at the same time as perovskite will have a steeper REE pattern and slightly lower REE because of a higher $K_{hib,LREE}/K_{hib,HREE}$ ratio and lower $K_{hib,REE}$ in hibonite (Kennedy et al., 1994), and thus a perovskite-hibonite mix undergoing dissolution will produce similar effects to the dissolution of just perovskite, but with a more marked increase of LREE/HREE ratios in the melt and crystallizing melilite. Since hibonite contains only small percentages of Ti when compared with perovskite, there are no tight constraints on the amount of hibonite that could have been present in the precursor to 3655A. The absence of trace-element-rich hibonite inclusions within melilite makes the suggestion of precursor hibonite tenuous at best and leaves any model involving hibonite dissolution poorly constrained. We have, therefore, focused on models dealing with the dissolution of perovskite to see how good a fit can be achieved without invoking the presence of hibonite.

6.2. Distribution and Size of Precursor Perovskite

The distribution of relict materials prior to dissolution is constrained largely by inference since the absence of a phase in any particular region of an inclusion does not preclude the possibility that it was originally present and that its dissolution controlled the concentration of trace elements in the melt during crystallization. Perovskite does occur in 3655A, though limited to a scattered distribution of small grains (<20 μm) in the outer half of the melilite-rich mantle. The original distribution and abundance are unknown but the bulk TiO_2 content of 1.2–1.8 wt% TiO_2 (Mason and Taylor, 1982; Wark and Lovering, 1982) imposes an upper limit of 2.0–3.0 wt% perovskite in the precursor. This amount of perovskite is sufficient to incorporate ~55–85% of the total REEs (excluding Eu), if average REE concentrations in precursor perovskite are equal to the maximum values measured in perovskite in 3655A (Table 4) and the bulk enrichment of the REEs in 3655A is 20 × ch, a value typical of CAIs.

Similar results are obtained from a consideration of REE crystal/melt partitioning. The first crystallizing melilite in 3655A (X_{Ak} ~ 0.05) has equilibrium crystal-liquid partition coefficients ranging from ~0.9(Er) to ~1.8(La), based on extrapolations of the semi-empirical expressions of Beckett et al. (1990) for Tm and La. The melilite in 3655A with X_{Ak} ~0.05 contains 1.2 ppm La and 0.7 ppm Er (Table 2, analysis 2–7) and, therefore, the coexisting melt contained ~0.8 ppm Er and ~0.7 ppm La. When melilite first began to crystallize, the droplet consisted mostly of melt with perhaps 10 wt% spinel and a small amount of perovskite. The spinel contains virtually no REEs, so perovskite and melt accounted for the entire REE budget of the droplet. Based on the assumption of a homogeneous melt with 0.7 ppm La and 0.8 ppm Er, a homogeneous perovskite with 130 ppm La and 79 ppm Er (Table 4), 20 × ch bulk enrichment of the REEs (corresponding to 4.7 ppm La and 3.2 ppm Er), and 10% crystallization of spinel prior to the appearance of melilite, mass balance then implies that 12% of the La and 21% of the Er resided in the liquid phase. Hence, 79(Er)–88(La)% of the bulk REEs were in perovskite during the initial stages of melilite crystallization. The above calculations are illustrative, but it is not unreasonable to conclude that perovskite, or possibly a mixture of perovskite and some other precursor, was a major carrier of REEs in the precursor to 3655A, incorporating more than half of the total REEs, and that the dissolution of perovskite played a major role in the development of the observed trace element distributions.

6.3. Dissolution of Relict Perovskite in 3655A

Previous work on the assimilation of foreign material into melts has assumed either a constant ratio of dissolution to crystallization rate or an open system (Neumann et al., 1954; DePaolo, 1981). Neither assumption is strictly applicable to the dissolution of relict material in Type B1 CAIs because the inclusions are essentially closed systems during crystallization due to formation of the melilite mantle, and it is unlikely that relative rates of dissolution and growth will remain constant during cooling. Kennedy and Edwards (1991) provide differential equations describing the case in which the rates of dissolution and crystallization are different, and partition coefficients are allowed to vary during crystallization. For the case of interest here, they assume (1) fractional crystallization of a trace element-bearing phase, (2) diffusively controlled dissolution (see Zhang et al., 1989), and (3) disequilibrium with a fixed concentration of the element of interest in the dissolving phase (i.e., The crystal buffers the trace element concentration in the melt only at the crystal-liquid interface and the crystal does not diffusively homogenize with respect to its trace element distribution during the dissolution process). The following equations (Kennedy and Edwards, 1991) can be evaluated numerically to model concentrations of trace elements in the melt, c_m, as crystallization proceeds. If the composition of the perovskite is constant, then

$$\frac{dc_m}{dy} = \frac{C_d}{F(y)}\left(F'(y) + m_f^*\right) - \left(F'(y) + m_f^* K_{\mathrm{mel},i}[F(y)]\right)\frac{c_m}{F(y)} \quad (1)$$

where c_m at time $t = 0$ is $(C_0 - C_d M_d)/F_0$, C_d is the fixed concentration of element i in the perovskite, and $y = t/t^*$. The dependence on time, t, is eliminated by using the equation:

$$F(y) = 1 - m_f^* - M_d(1 - \sqrt{y}) \quad (2)$$

to calculate F for a given value of y. We have used * to denote the value of a parameter at the instant complete dissolution occurs. Thus, y changes from 0 to 1 during dissolution.

In the above equations, F is the melt fraction, F', the derivative of F with respect to y: C_0 is the bulk concentration of element i, F_0, the initial melt fraction, M_d, the mass fraction of the dissolving phase, $K_{\mathrm{pv},i}$, the partition coefficient of element i at the interface between the dissolving perovskite and melt, $K_{\mathrm{mel},i}$, the crystal-liquid partition coefficient of element i for the crystallizing melilite, and m_f^*, the total mass fraction that has crystallized at the instant dissolution stops. Once dissolution is complete, we use the following equation to calculate c_m,

$$c_m = c_m^* \left[\frac{F}{F^*}\right]^{K_c - 1} e^{K_m(F - F^*)} \quad (3)$$

where K_m and K_c are the constants in the equation of Beckett et al. (1990) that describe variations in the partition coefficient of the crystallizing melilite ($K_{\mathrm{mel},i} = K_m F + K_c$). For 3655A, we used these equations to calculate La distributions as a function of X_{Ak} in melilite crystallizing from the 3655A precursor liquid, assuming $K_{\mathrm{mel,La}} = 4.50\mathrm{F} - 2.70$ and $X_{\mathrm{Ak}} = 0.019/(F - 0.521)$. These relationships are slightly different to those given by Beckett et al. (1990) as we have assumed that (1) there was 10% spinel prior to dissolution of perovskite and crystallization of melilite; (2) spinel co-crystallized with melilite during crystallization of the mantle such that the "solid extract" at any given time consisted of 8 wt% spinel and 92 wt% melilite; (3) no other phase crystallized in sufficient quantity to affect our calculations; (4) the amount of relict perovskite is 4% of the mass of the inclusion; and (5) complete dissolution of any perovskite grains held in contact with melt occurs by the time the inclusion is 45% crystallized, that is, by the time the melilite mantle has formed. Thus, $M_d \cong 0.04$ and $F^* = 0.55$ for the bulk CAI. These assumptions are based on the phase equilibria experiments of Stolper (1982), Stolper and Paque (1986), and Beckett et al. (1990), the bulk composition of 3655A, and our observations as discussed above. The above equation for $K_{\mathrm{mel,La}}$ in 3655A and the $K_{\mathrm{mel,La}}$ equations in the caption for Fig. 9 use C_0, M_d, m_f^*, and F^* values adjusted for the 10% spinel present prior to the initiation of melilite crystallization and perovskite dissolution.

Figure 9 compares the measured La concentrations in 3655A melilite with the calculated La concentration profiles for three different scenarios: (A) Only melilite + spinel crystallize. (B) Crystallization of melilite and spinel is accompanied by diffusive dissolution of perovskite. Perovskite does not equilibrate with the melt and has a fixed La concentration of 128 ppm, leading effectively to a decreasing $K_{\mathrm{pv,La}}$ as melilite crystallizes. (C) A linear relationship between F and X_{Ak}, $X_{\mathrm{Ak}} = 1.7145 - 1.9355F$, has been used with the same assumptions as model B. Curve A shows no resem-

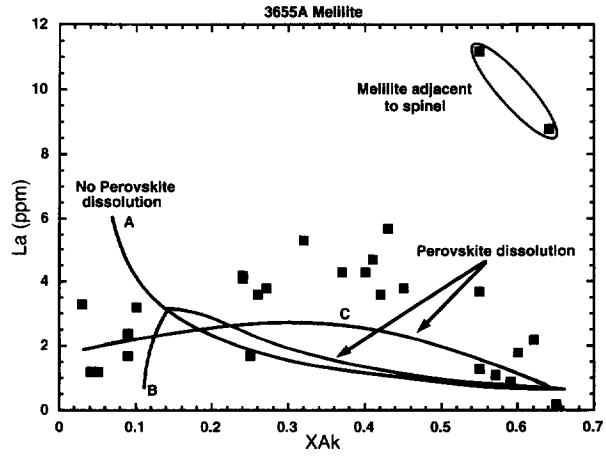

Fig. 9. Lanthanum concentration in melilite from 3655A. The bulk inclusion is assumed to have 20xch La. Curves are calculated La concentrations for melilite (A) in a perovskite-free inclusion, (B) with dissolution of 4% perovskite whose La concentration is fixed at 128 ppm, and (C) with dissolution of perovskite as for B, but with a linear relationship between X_{Ak} and F. Melilite partitioning is described by $K_{\mathrm{mel,La}} = 4.501F - 2.701$ in model A and by $K_{\mathrm{mel,La}} = 5.0739F - 3.0507$ in models B and C. The relationship between X_{Ak} and F is $X_{\mathrm{Ak}} = 0.019/(F - 0.521)$ for A and B, and for model C, $X_{\mathrm{Ak}} = 1.7145 - 1.9355F$. Concentrations of La in melilite were calculated using the equations of Kennedy and Edwards (1991) for dissolution accompanied by crystallization with varying partition coefficients in the crystallizing phases (see text).

blance to the 3655A melilite data and this model can be discarded. Model B exhibits two essential features of the 3655A data. Lanthanum is low for both gehlenitic and akermanitic melilite, and a La maximum occurs for intermediate X_{Ak}. In detail, however, the agreement is poor due to the very rapid initial rate of dissolution required to generate the rapid initial increase in La. In model B, fifty percent of the available perovskite dissolves during the first 10% of melilite crystallization. If perovskite dissolution is delayed or if perovskite grains are more highly concentrated in a shell within the proto-CAI, the maximum La concentration in melilite will shift to higher X_{Ak}, but the agreement with observed La profiles in 3655A melilite will still be poor. The length of the La concentration pulse in melilite reflects the relationship between X_{Ak} and F that is used. The importance of this relationship to the length of the La pulse is shown by model C. When X_{Ak} is linearly related to F, rather than to $1/F$, there is a dramatic lengthening of the La pulse in Figure 9. Model C provides a curve that mimics the La vs. X_{Ak} relationship observed in the 3655A data, but it requires a relationship between F and X_{Ak} that is different from the relationship given by Beckett et al. (1990). This may reflect localized enrichment of La in the melt or an additional process that affects partitioning of La into melilite.

Another test of perovskite dissolution models is to examine LREE/HREE ratios (e.g., La/Dy, Fig. 6c) in melilite. The increase of the melilite La/Dy as crystallization proceeds (Fig. 6c) is difficult to model with perovskite dissolution for the following reasons: (1) the chondrite normalized (La/Dy) ratio of perovskite in 3655A is close to 1.0 and addition of perovskite to the melt will not rotate a chondrite normalized melilite REE pattern significantly, and (2) the $K_{mel,La}/K_{mel,Dy}$ ratio for melilite is essentially constant in the experiments of Beckett et al (1990) and, thus, rotation of the REE pattern should not occur if melilite is the only phase crystallizing. A number of alternative processes or effects can be suggested that may have had a role in the observed increase of La/Dy in melilite: (1) dissolution of perovskite with a chondrite normalized (La/Dy) of 3, a value consistent with all experimental partitioning studies of perovskite, (2) dissolution of a mixture of perovskite and hibonite, which is likely to have a higher La/Dy than perovskite alone, as hibonite has a higher a $K_{mel,La}/K_{mel,Dy}$ ratio (>15) than perovskite (Kennedy et al., 1994), (3) increasing $K_{mel,La}/K_{mel,Dy}$ in melilite as crystallization proceeds, (4) early onset of the crystallization of clinopyroxene, a phase that preferentially accepts Dy over La, and/or (5) early crystallization of melilite into a partially volatilized Mg-, Si-depleted region near the surface of the cooling droplet. These liquids would be zoned in the REEs as well as the major elements due to their different activity-composition relations as a function of the liquid composition (e.g., Richter, 1993). If both LREEs and HREEs achieved constant activities within these zoned liquids, then the LREE/HREE concentration ratio would vary as a function of position in a way that reflected the inverse of the LREE/HREE activity coefficient ratio. It is possible that melilite crystallizing from these anomalous liquids could have a lower than expected apparent $K_{mel,La}/K_{mel,Dy}$ because the melt had a nonhomogeneous distribution of the REEs, and the relationship between X_{Ak} and degree of crystallization used in model calculations, which are based on equilibrium fractional crystallization, would be in error. A related complication would arise if there were an evaporation condition for the REEs at the surface of the droplet. Further detailed studies of Type B1, all of which exhibit this unexpected increase of La/Dy in melilite, are required before the applicability of these alternatives can be assessed.

The calculated La zoning profiles for melilite crystallizing with the simultaneous dissolution of perovskite share features in common with the La distributions measured in 3655A. Nevertheless, perovskite dissolution, or dissolution of a mixture of perovskite and other plausible precursor phases, cannot account for the observed enrichments of Ba in melilite (Ba concentrations in perovskite are low, 16–40 ppm) or the enrichment of trace elements in melilite adjacent to included spinel and pyroxene. It is possible that the high La concentrations of melilites in 3655A reflect a changing mass fraction (M_d) of perovskite undergoing dissolution and contributing REEs to the melt from which melilite crystallized. However, the enrichment of REEs adjacent to spinel inclusions and in melilite with intermediate akermanite contents is not accompanied by enrichments of Ti, as might be expected if a Ti-rich phase were dissolving (Burnett et al., 1990). Thus, dissolution of a trace-element-rich precursor material, such as perovskite or a mixture of perovskite and hibonite, must be accompanied by one or more additional controls on partitioning, such as interface kinetics, chemical boundary layers, and/or nucleation of accessory phases, that also affect the distribution of trace elements. In the next section, we examine the consequences of trace-element-enriched boundary layers during crystallization of Type B1 CAIs.

7. TRACE ELEMENT ENRICHED BOUNDARY LAYERS

In previous sections, we argued that dissolution of perovskite influenced trace element abundances in melilite from Type B1 inclusions but that additional factors also played a role. Interface kinetics and diffusion have been invoked to explain differences in trace element abundances in the different sectors of sector zoned clinopyroxene (Shimizu, 1981; Watson and Liang, 1995), small inclusions of clinopyroxene in CAI melilite and plagioclase (Barber et al., 1984), and the presence of chemical gradients adjacent to crystals. In terrestrial systems, chemical boundary layers are typically <10 μm in thickness because convection prevents the development of large chemical gradients (Bacon, 1989), but in Soret and diffusive dissolution experiments where convection is inhibited (Lesher and Walker, 1986; Zhang et al., 1989), chemical gradients in both major and trace elements can develop over millimeter-scale distances. Convection is less likely to occur in a zero gravity environment than in a terrestrial environment, and large chemical boundary layers may develop in CAIs in response to rapid crystal growth or vaporization at the droplet surface. Soret diffusion is less likely to occur as it requires large temperature gradients, typically hundreds of degrees, to be maintained for more than a day (Lesher and Walker, 1986).

Albaréde and Bottinga (1972) introduced kinetic models to describe the development of a trace-element-enriched boundary layer during crystal growth and its effect on trace element partitioning. Their equations are not strictly applica-

ble to Type B1 CAIs because equilibrium partition coefficients (K_{Eq}), ratios of diffusion coefficient to growth rate, and distances between the centers of growing crystals were all assumed to remain constant. It is, nevertheless, useful to examine the crystallization of Type B1 CAI using their approach. Albaréde and Bottinga defined an apparent partition coefficient, K_{App}, as the ratio of the concentration of a trace element in the surface layer of the crystallizing solid to the concentration in the melt beyond the boundary layer. If the concentration in the liquid boundary layer at the crystal/liquid interface differs from the bulk melt, then $K_{App} \neq K_{Eq}$. Albaréde and Bottinga also define a term, alpha (α), as the ratio of the diffusion coefficient of the element of interest in the melt to the crystal growth rate, multiplied by the dimension of the reservoir. Alpha is a measure of kinetic disequilibrium; the smaller α is, the greater the difference between the apparent partition coefficient and the equilibrium partition coefficient.

We can use literature diffusion data and melilite growth rates derived from estimated cooling rates and the typical size of melilite in the mantle of 3655A to calculate a probable range for K_{App} in melilite. Average growth rates are $2-5 \times 10^{-6}$ cm/s for cooling rates between 50 and 100°C/h over a 200°C temperature interval (Stolper and Paque, 1986) and a 350 μm melilite crystal length. Diffusion rates within the melt at temperatures between 1250 and 1450°C are probably in the range 10^{-6} to 10^{-8} cm^2/s (Hofmann, 1980; Freer, 1981). For a 0.5 cm reservoir length, α is therefore in the range of 0.001–0.25, and boundary layers can be expected to develop. If, for example, $\alpha = 0.01$, then K_{App} for an incompatible element increases rapidly during the first 10–20% of crystallization, and subsequently remains relatively constant (see Albarede and Bottinga, 1972: Fig. 7 for an example with $K_{Eq} = 0.5$). For the trivalent REEs, this effect competes with a decrease in K_{Eq} of melilite as crystallization proceeds (Beckett et al., 1990). When the rate of increase of K_{App} exceeds the rate of decrease of K_{Eq}, the concentration of the element in the crystallizing melilite will increase and vice versa. However, only for high cooling rates, possibly close to the upper value of 100°C/hr assumed above, is it likely that the increase in K_{App} for trivalent cations can exceed the dramatic rate of decrease in K_{Eq} due to crystal chemical effects sufficiently to account for the observed REE enrichments. Additional data on trace element abundances in boundary layers adjacent to spinel included in melilite are also needed, but our reconnaissance study clearly demonstrates the existence of enrichments near spinel inclusions, extending well beyond 50 μm in some instances. Models of trace element partitioning in Type B1 CAIs must, therefore, consider the effect of boundary layers at the front of the crystallizing melilite mantle.

The development of a trace element enriched boundary layer cannot explain the low REE content of early, low Ak melilite as the partition coefficient of low Ak melilite is ~1.0, and the closer a partition coefficient is to 1.0, the less the enrichment within a boundary layer (Albarede and Bottinga, 1972). Thus, retention of REEs by perovskite during the initial stages of crystallization is still required to explain the low initial concentrations of REEs in melilite. The combination of dissolution of relict material and boundary-layer induced trace element enrichments is the most plausible explanation of the distribution of trace elements in 3655A, and, by inference, in other Type B1 CAIs.

8. MAGNESIUM ISOTOPE RECORD

The Mg isotope record of 3655A is distinguished by four salient features: (1) large ^{26}Mg excesses correlated with the respective Al/Mg ratios in plagioclase, melilite, and hibonite, (2) mass-dependent fractionation favoring the heavier Mg isotopes in all primary phases, (3) a heterogeneous distribution of F_{Mg} values with F_{Mg} in melilite systematically greater than in either spinel or fassaite, and (4) isotopically normal Mg in the secondary alteration phases, grossular and monticellite. The presence of radiogenic ^{26}Mg* with ^{26}Mg*/^{27}Al $\sim 5 \times 10^{-5}$ and of mass-dependent fractionation with $F_{Mg} > 0$ are characteristic features of coarse-grained CAI in C3V chondrites (Hutcheon, 1982; Niederer and Papanastassiou, 1984; Podosek et al., 1991; Goswami et al., 1994). While none of these features, taken individually, are unexpected in CAIs, the presence of all of these features is unique among CAIs studied thus far and places stringent constraints on the thermal history of 3655A. In this section, we discuss the Mg isotope data and outline a model for the formation of 3655A which best explains both the trace element and isotope features. This model includes (1) flash heating to partially melt a precursor characterized by a mean F_{Mg} value of ~4‰/amu, (2) rapid cooling to preserve relict spinel and perovskite, (3) diffusive exchange of Mg between melilite and a nebular reservoir enriched in the heavier Mg isotopes, and (4) secondary alteration at low temperature leading to the formation of grossular and monticellite.

8.1. Heterogeneity in F_{Mg}

In a simple one-stage model involving crystallization from a homogeneous melt and in the absence of post-crystallization alteration, F_{Mg} values should be identical in all phases. The heterogeneity of F_{Mg} values among spinels (Fig. 4b) and the systematic difference in F_{Mg} between melilite and the other minerals (Fig. 4c,d), indicate that 3655A must have had a more complex history. The variation in F_{Mg} among spinels in 3655A is similar to that observed in Purple, Spinel-rich refractory Inclusions (PSI; Brigham et al., 1988) and in plagioclase-olivine Inclusions (Sheng et al., 1991), although reduced in magnitude. As discussed by Sheng et al. (1991), this heterogeneity in F_{Mg} is most plausibly explained by the presence of relict spinels which have retained their original Mg isotope compositions and have not equilibrated isotopically with the silicate melt due to incomplete melting and rapid cooling of the host CAI. In the context of the flash heating model presented by Sheng et al. (1992), the survival of relict spinel in 3655A with distinct Mg isotopic compositions can be used to constrain the thermal history. Using the estimate of T_{max} discussed above, 1450°C $< T_{max} <$ 1574°C, and an average 20 μm spinel radius in Eqn. 16c of Sheng et al. (1992), we calculate minimum cooling rates of 9–63°C/h. Slower cooling would allow diffusive equilibration of Mg between spinel and the melt, contrary to the observations. This range of cooling rates is fully consistent with those deduced from experimental studies of CAI textures and mineralogy (MacPherson et al., 1984; Stolper and Paque, 1986).

While the survival of relict phases appears to provide a plausible explanation for REE abundances in early-crystallizing melilite and for the variation in F_{Mg} among spinels, it cannot account for the small, but clearly resolved, difference in F_{Mg} values between melilite (mean F_{Mg} = 5.3 ± 0.5‰/amu) and both spinel (mean F_{Mg} = 3.3 ± 0.5‰/amu) and fassaite (mean F_{Mg} = 3.6 ± 0.3‰/amu; uncertainties in the mean F_{Mg} values are twice the standard error of the mean). This observation identifies 3655A as the first CAI in which melilite and fassaite are both homogeneous with respect to F_{Mg} (i.e., within both phases, all F_{Mg} values fall within two standard deviations of the mean), but in which the mean F_{Mg} value for melilite is distinctly higher than the mean F_{Mg} value for fassaite. We suggest that the simplest model compatible with these data involves crystallization of both fassaite and melilite from a melt with $F_{Mg} \sim$ 3.5‰/amu. Melilite subsequently acquired its distinctive F_{Mg} value through diffusive reequilibration with a gaseous nebular reservoir enriched in the heavier Mg isotopes. A model of this type requires rapid diffusion of Mg in melilite, over distances approaching 1 mm, while spinel and fassaite retain, for the most part, their original Mg isotope compositions. In this regard, we suggest that the Mg isotope record in 3655A is the product of diffusion-controlled isotope exchange in a manner analogous to that believed responsible for the heterogeneous distribution of O isotopes in CAIs (Clayton et al., 1977; Ryerson and McKeegan, 1994).

In principle, the ability of this model to account for the observed Mg isotope record in 3655A can be evaluated using the respective diffusion parameters for the constituent CAI phases. While Mg self-diffusion in spinel has been well characterized by Sheng et al. (1992), only very limited data are available for melilite and clinopyroxene. Diffusion of Mg in clinopyroxene is very sluggish. From the failure to observe a measurable diffusion profile, Freer et al. (1982) set an upper limit on the Mg diffusion coefficient in diopside at 1250°C, $D_{Di,Mg}$ (1250°C), of 7×10^{-14} cm^2/s. The diffusion of Mg in melilite has not been measured directly, but based on a determination of the diffusion coefficients of other divalent cations, Morioka and Nagasawa (1991) estimated a Mg self-diffusion coefficient in åkermanite at 1200°C, $D_{Mel,Mg}$ (1200°C), of $\sim 1 \times 10^{-12}$cm^2/s, comparable to that measured in spinel. Activation energies for Mg diffusion in melilite and diopside have not been determined.

In the absence of a self-consistent set of Mg diffusion parameters for melilite and fassaite, the ability of the model to explain the Mg isotope record in 3655A cannot be evaluated quantitatively. Rather, following the approach used by Ryerson and McKeegan (1994) to discuss O diffusion in these same CAI phases, we estimate relative diffusion rates for melilite and fassaite consistent with the basic premise of our model—that the heterogeneous distribution of F_{Mg} values in 3655A reflects subsolidus diffusion of Mg. The fractional degree of Mg isotope equilibration among the various CAI phases is sensitive to the ratio of effective diffusion dimensions, e.g., a_{Mel}/a_{Sp} for melilite and spinel. Thus, small differences in diffusivity among minerals may be compensated by differences in diffusion path length. For example, melilite and fassaite in 3655A have comparable petrographic grain sizes, $a_{Mel}/a_{Cpx} \sim 1$, and the disparity in F_{Mg} values is consistent with more sluggish Mg diffusion in clinopyroxene. On the other hand, average grain sizes of melilite and spinel are very different (a_{Mel}/a_{Sp} ratios can be as high as ~50) and this generates serious difficulties for an analogous interpretation of the difference in F_{Mg} values between these phases. If, as suggested by Morioka and Nagasawa (1991), the Mg diffusion rate in melilite at high temperatures (~1200°C) is comparable to that in spinel and if the respective diffusion lengths are approximately equal to the petrographically observed grain sizes, then spinel in 3655A would approach complete equilibration much faster than melilite. This expectation is clearly contrary to our observations for 3655A. Thus, a diffusive exchange model can explain the distribution of F_{Mg} values in 3655A only if either the effective diffusion length in melilite is much less than the petrographic grain size, and/or the actual self-diffusion rate of Mg applicable to melilite in Type B CAI is much higher than the rate estimated by Morioka and Nagasawa (1991).

The tendency for melilite to exhibit much more pronounced microcracking along cleavage planes than either spinel or fassaite provides some evidence that the length scale for diffusion can be less than the observed grain size (see, e.g., Kim et al., 1992). Moreover, melilite in nearly all Allende Type B inclusions is crosscut by alteration veins, providing evidence of the diffusive transport of Ca and Si in CAIs on length scales much less than the petrographic grain size of melilite. According to equilibrium condensation calculations, Mg is not volatile at low temperatures in a gas of solar composition (Grossman, 1972), and this is true even if the H/O ratio of the vapor is greatly enhanced (e.g., Hashimoto, 1992). On the basis of mass balance and textural arguments (Wark, 1981; Hashimoto and Grossman, 1987), however, Mg condensed during the alteration process, implying significant concentrations of Mg in the altering fluid. Possibly, this simply means that the altering vapor was not a gas of solar composition. On balance, we conclude that the requirements of the diffusive exchange model are not unreasonable and that this scenario provides the most plausible explanation for the heterogeneous F_{Mg} distribution in 3655A.

In a study of O self-diffusion rates, Ryerson and McKeegan (1994) concluded that a "dynamic exchange" model, involving diffusive exchange during partial melting and resolidification, provides the best fit to the oxygen isotope record in Type B CAIs. By allowing rapid exchange of O between the melt and a nebular reservoir prior to and during crystallization of melilite, this scenario produces good agreement between the predicted isotopic compositions of spinel, anorthite, and melilite and the observations. Discrepancies between the expected and observed oxygen isotope composition of fassaite, however, remain unresolved and oxygen isotope compositions of a plagioclase crystal from CAI 3529Z measured in situ using SIMS by McKeegan et al. (1996) are difficult to reconcile with a simple diffusion model. Application of a "dynamic exchange" model to Mg in 3655A encounters similar problems. We assume rapid heating to T_{max}, leaving relict spinel and perovskite immersed in an isotopically homogeneous silicate melt. As cooling proceeds, the melt undergoes Mg isotopic exchange with a reservoir characterized by $F_{Mg} \sim$ 6‰/amu. Crystals grown from the melt assume the isotopic composition of the melt at the time of crystallization. While providing a plausible

explanation for the difference in F_{Mg} between melilite and spinel without requiring fast Mg diffusion in melilite, the model does not plausibly account for the disparity in F_{Mg} between fassaite and melilite. Since pyroxene always crystallizes after melilite in Type B CAIs (Stolper and Paque, 1986), the F_{Mg} values in fassaite should be equivalent to those in melilite unless the composition of the reservoir changed prior to the onset of pyroxene crystallization. Even if this were the case, however, measurable zonation in F_{Mg} would be expected in melilite and/or fassaite.

Before leaving this discussion of Mg isotope exchange in 3655A, it is worthwhile to consider the possibility that processes other than diffusion may play an important role establishing the distribution of Mg isotopes among the coexisting CAI phases. Recent studies have demonstrated convincing links between the degree of isotopic disturbance and petrographic evidence of alteration and recrystallization and many CAIs appear to have experienced multiple episodes of metamorphism and partial melting (e.g., Podosek, 1991; MacPherson and Davis, 1993). It is unlikely the full story of inclusions like 3655A can be revealed without a more thorough understanding of the behavior of Mg during these episodes and without additional laboratory measurements of the Mg diffusion parameters for fassaite and melilite.

8.2. Al-Mg Isotope Systematics

The abundance of radiogenic $^{26}Mg^*$ in melilite and plagioclase indicates early crystallization of 3655A, while ^{26}Al was still extant at approximately the canonical solar system value of $^{26}Al/^{27}Al \sim 5 \times 10^{-5}$. Inclusion 3655A appears to have formed contemporaneously with most other Type B1 inclusions. The data in Fig. 5 show little indication for disturbance of the Al-Mg system; data from all four anorthite crystals and seven of eight melilites lie within two standard deviations of the line fitted to the data. Both the petrographic evidence (Paque, 1990) and the ^{26}Al-^{26}Mg isotope systematics thus indicate that secondary alteration in 3655A was restricted to fractures and grain boundaries, leaving the interiors of melilite and anorthite crystals relatively undisturbed, at least with respect to the ^{26}Al-^{26}Mg system. 3655A is, in this sense, similar to the Allende Type B CAI Egg 3 (Armstrong et al., 1984) and 3529Z (Podosek et al., 1991). Data from hibonite in the rim of the inclusion also lie on the line fitted to the anorthite-spinel data, suggesting that rim formation was contemporaneous with crystallization of the host CAI and must have occurred prior to significant decay of ^{26}Al, i.e., within ~0.1 Ma.

In contrast to melilite, anorthite, and hibonite, no evidence of radiogenic $^{26}Mg^*$ was found in grossular. Despite $^{27}Al/^{24}Mg$ ratios of up to 50, calculated $^{26}Mg^*/^{27}Al$ ratios are $<1.5 \times 10^{-5}$. Hutcheon and Newton (1981) noted a similar absence of $^{26}Mg^*$ in grossular in the Allende Type B1 CAI TS-23 and, based on thermochemical and petrographic arguments, proposed that grossular formed at low temperature (<685°C), via the closed system reaction, melilite + anorthite = grossular + monticellite. In this model, the absence of $^{26}Mg^*$ was interpreted chronologically to indicate formation of grossular at least 2.4 Ma after crystallization of the host inclusion. A recent modification to the Hutcheon and Newton model, based on trace element distributions in TS-23, suggests grossular and monticellite formed largely from åkermanitic melilite by reaction with an SiO_2-bearing fluid with only a minor contribution from anorthite (Davis et al., 1994). Secondary minerals in TS-23 appear to have inherited their trace element (and Mg isotope) abundances from melilite without experiencing wholesale exchange of components with an external reservoir. In 3655A, however, the difference in F_{Mg} values between primary melilite ($F_{Mg} \sim 5$‰/amu) and secondary grossular and monticellite ($F_{Mg} \sim 0$) in 3655A indicates that the growth of secondary minerals in 3655A involved extensive exchange of Mg with an isotopically normal reservoir. This evidence of open-system behavior for Mg precludes the use of the ^{26}Al-^{26}Mg chronometer as an unambiguous indicator of the timescale of alteration. If we assume that alteration occurred late, following the decay of ^{26}Al, as suggested by Hutcheon and Newton (1981) and Davis et al. (1994), then the absence of $^{26}Mg^*$ in grossular can be interpreted chronologically to reflect an interval of at least 1 Ma between CAI crystallization and the growth of secondary phases. Alternatively, alteration may have commenced early, while ^{26}Al was still relatively abundant. In this case, all evidence of $^{26}Mg^*$ in the fine-grained secondary phases would be subsequently removed by subsolidus Mg isotope exchange. While the data do not allow either possibility to be excluded unequivocally, we regard late formation as the more plausible alternative.

9. FORMATION OF 3655A

Our model for the evolution of 3655A includes the following sequence of events: (1) condensation of precursor phases from a nebular reservoir enriched in the heavier Mg isotopes ($F_{Mg} \sim 3.5$‰/amu), (2) aggregation of these crystalline materials, which includes REE-rich perovskite, to form the precursor Type B1 CAI (the intimate association of spinel and perovskite in the small spinel palisade suggests a cogenetic relationship for these phases), (3) partial melting of the 3655A precursor during a short duration thermal pulse (the combination of T_{max} below the melting point of perovskite and a short heating interval prevented complete dissolution of perovskite and spinel before the initiation of melilite crystallization), (4) rapid cooling, with a minimum cooling rate between 10 and 60°C/h, and initiation of melilite crystallization at the rim of the inclusion. Dissolution of perovskite, and possibly other precursor phases, continues during melilite crystallization, producing a rapid increase of REE concentrations in the melt until dissolution stops. Crystallization of melilite was sufficiently rapid to trap partially dissolved perovskite and to produce growth rates consistent with the formation of trace element enriched boundary layers at the melilite-melt interface. The enrichment of Ba in melilite and the localized enrichments of trace elements in boundary layers around spinel included in melilite and pyroxene are a consequence of this rapid growth, (5) partial re-equilibration of melilite, but not fassaite or spinel, with a nebular reservoir to produce the observed heterogeneity in F_{Mg}, and (6) subsolidus alteration along grain boundaries in the melilite-rich mantle to produce grossular and monticellite containing isotopically normal Mg, $F_{Mg} \sim 0$, and no radiogenic $^{26}Mg^*$.

10. CONCLUSIONS

The distribution of trace elements in melilite from the mantle of 3655A is unlike the distribution predicted from the experiments of Beckett et al. (1990) in terms of absolute concentrations, concentration ratios, and concentration profiles. Lanthanum concentrations are lower than expected in the first crystallized, low Ak melilite, rapidly increase to higher than expected concentrations in intermediate Ak melilite, and only then decrease as expected. Barium concentrations are 10–50 times higher than expected, and the LREE/HREE ratio increases continuously rather than remaining constant. In addition, there are large trace element enrichments adjacent to included spinel in both melilite and clinopyroxene, requiring the development of trace element enriched boundary layers. In general, trace element abundances in melilites from 3655A reflect the dual influence of dissolution of a trace element-rich precursor material, such as perovskite, or possibly a mix of perovskite and hibonite, and, trace element enriched boundary layers due to rapid crystal growth and fast (~100°C/h) cooling rates.

The distribution of Mg isotopes in 3655A is similarly inconsistent with simple closed-system crystallization from a homogeneous melt. The heterogeneity in F_{Mg} is most plausibly explained by partial melting of a mixed silicate-oxide precursor assemblage, characterized by a mean F_{Mg} of ~4‰/amu and a $^{26}Al/^{27}Al$ ratio of $\sim 4 \times 10^{-5}$, followed by rapid cooling and then diffusive exchange of Mg in melilite. The well-defined ^{26}Al-^{26}Mg correlation imposes a short timescale, <0.1 Ma, for these events. Alteration of melilite to form grossular and monticellite occurred at much lower temperature, <800°C, and probably much later. The patchy distributions of TiO_2 in the cores of clinopyroxene, a unique feature of 3655A, does not indicate survival of relict fassaite but reflects superimposed precursor textural characteristics and the effects of rapid crystallization.

The combined isotope and trace element data for 3655A point to a complex, multi-stage evolution for the inclusion and underscore the need to determine the isotopic and chemical characteristics precisely and with micrometer spatial resolution in order to decipher correctly the petrogenetic history. Many other CAIs exhibit features similar to those reported here (e.g., Podosek et al., 1991; MacPherson and Davis, 1993; Goswami et al., 1994), and we believe that nearly all refractory inclusions experienced prolonged nebular evolution. Differences in the degree of homogeneity in the isotopic and trace element records among inclusions are most plausibly attributed to differences in thermal history. Improved data on diffusion rates of Mg, Si, and REEs are required to model more precisely and realistically CAI thermal histories and the nebular environment they reflect.

Acknowledgments—This work was supported by NASA grants NAG 9-43, NAGW-3297, NAGW-3533, NAG 9-105, and performed under the auspices of the DOE by LLNL under contract W-7405-Eng-48. The thin section of USNM 3655A was graciously provided by G. J. MacPherson. We thank Julie Paque, Frank Richter, and Ed Stolper for insight and helpful suggestions, and Ahmed El Goresy, Hiroshi Nagasawa and two anonymous reviewers for very constructive comments. Division Contribution #5161(780).

Editorial handling: R. A. Schmitt

REFERENCES

Albarede F. and Bottinga Y. (1972) Kinetic disequilibrium in trace element partitioning between phenocrysts and host lava. *Geochim. Cosmochim. Acta* **36,** 141–156.

Anders E. and Grevesse N. (1989) Abundance of the elements: Meteoritic and solar. *Geochim. Cosmochim. Acta* **53,** 197–214.

Armstrong J. T. (1982) New ZAF and α-factor correction procedures for the quantitative analysis of individual microparticles. In *Microbeam Analysis*/1982 (ed. K. F. J. Heinrich), pp. 175–180. San Francisco Press.

Armstrong J. T. (1984) Quantitative analysis of silicate and oxide minerals: A re-evaluation of ZAF corrections and proposal for new Bence-Albee coefficients. In *Microbeam Analysis*/1984 (ed. A. Romig and J. I. Goldstein), pp. 208–212. San Francisco Press.

Armstrong J. T., Hutcheon I. D., and Wasserburg G. J. (1984) Disturbed Mg isotopic systematics in Allende CAI. *Lunar Planet. Sci.* **XV,** 15–16 (abstr.).

Armstrong J. T., Hutcheon I. D., and Wasserburg G. J. (1987) Zelda and Company: Petrogenesis of sulfide-rich Fremdlinge and constraints on solar nebula processes. *Geochim. Cosmochim. Acta* **51,** 3155–3173.

Bacon C. R. (1989) Crystallization of accessory phases in magmas by local saturation adjacent to phenocrysts. *Geochim. Cosmochim. Acta* **53,** 1055–1066.

Barber D. J., Martin P. M., and Hutcheon I. D. (1984) The microstructure of minerals in coarse-grained Ca-Al-rich inclusions from the Allende meteorite. *Geochim. Cosmochim. Acta* **48,** 769–783.

Beckett J. R. (1986) The origin of calcium-, aluminum-rich inclusions from carbonaceous chondrites: An experimental study. Ph.D. thesis, University Chicago.

Beckett J. R. and Stolper E. (1994) The stability of hibonite, melilite and other aluminous phases in silicate melts: Implications for the origin of hibonite-bearing inclusions from carbonaceous chondrites. *Meteoritics* **29,** 41–65.

Beckett J. R., Spivack A. J., Hutcheon I. D., Wasserburg G. J., and Stolper E. M. (1990) Crystal chemical effects on the partitioning of trace elements between mineral and melt: An experimental study of melilite with applications to refractory inclusions from carbonaceous chondrites. *Geochim. Cosmochim. Acta* **54,** 1755–1774.

Berman R. G. (1983) A thermodynamic model for multicomponent melts, with application to the system CaO-MgO-Al_2O_3-SiO_2. Ph.D. thesis, University British Columbia.

Blum J. D., Wasserburg G. J., Hutcheon I. D., Beckett J. R., and Stolper E. M. (1989) Origin of opaque assemblages in C3V meteorites: Implications for nebular and planetary processes. *Geochim. Cosmochim. Acta* **53,** 543–556.

Brigham C. A. (1990) Isotopic heterogeneity in calcium-aluminum rich meteoritic inclusions. Ph.D. thesis, California Institute of Technology.

Brigham C. A., Hutcheon I. D., Papanastassiou D. A., and Wasserburg G. J. (1988) Isotopic heterogeneity and correlated isotope fractionation in purple FUN inclusions. *Lunar Planet. Sci.* **XIX,** 132–133 (abstr.).

Burnett D. S., Johnson M. L., and Woolum D. S. (1990) Relict grains in CAIs, revisited. *Meteoritics* **25,** 353 (abstr.).

Chen J. H. and Wasserburg G. J. (1981) The isotopic composition of uranium and lead in Allende inclusions and meteoritic phosphates. *Earth Planet. Sci. Lett.* **52,** 1–15.

Clark A. M. (1984) Mineralogy of the rare earth elements. In *Rare Earth Element Geochemistry* (ed. P. Henderson), pp. 33–61. Elsevier.

Clayton R. N., Onuma N., Grossman L., and Mayeda T. K. (1977) Distribution of the pre-solar component in Allende and other carbonaceous chondrites. *Earth Planet. Sci. Lett.* **34,** 209–224.

Davis A. M. et al. (1991) Melt solidification and late-stage evaporation in the evolution of a FUN inclusion from the Vigarano C3V chondrite. *Geochim. Cosmochim. Acta* **55,** 621–637.

Davis A. M., Simon S. B., and Grossman L. (1992) Melilite composition trends during crystallization of Allende Type B1 refractory inclusion melts. *Lunar Planet. Sci.* **XXIII,** 281–282 (abstr.).

Davis A. M., Simon S. B., and Grossman L. (1994) Alteration of Allende Type B1 CAIs: When, where and how. *Lunar Planet. Sci.* **XXV,** 315–316 (abstr.).

DePaolo D. J. (1981) Trace element and isotopic effects of combined wallrock assimilation and fractional crystallization. *Earth Planet. Sci. Lett.* **53,** 189–202.

El Goresy A., Nagel K., and Ramdohr P. (1979) Spinel framboids and fremdlinge in Allende inclusions: Possible sequential markers in the early history of the solar system. *Proc. Lunar Planet. Sci. Conf. 10th,* 833–850.

El Goresy A., Armstrong J. T., and Wasserburg, G. J. (1985) Anatomy of an Allende coarse-grained inclusion. *Geochim. Cosmochim. Acta* **49,** 2433–2444.

Fahey A. J., Zinner E. K., Crozaz G., and Kornacki A. S. (1987) Microdistributions of Mg isotopes and REE abundances in a Type A calcium-aluminum-rich inclusion from Efremovka. *Geochim. Cosmochim. Acta* **51,** 3215–3229.

Freer R. (1981) Diffusion in silicate minerals and glasses: A data digest and guide to the literature. *Contr. Mineral. Petrol.* **76,** 440–454.

Freer R., Carpenter M. A., Long J. V. P., and Reed S. J. B. (1982) "Null result" diffusion experiments with diopside: Implications for pyroxene equilibria. *Earth Planet. Sci. Lett.* **58,** 285–292.

Goswami J. N., Srinivasan G., and Ulyanov A. A. (1994) Ion microprobe studies of Efremovka CAIs: I. Magnesium isotope composition. *Geochim. Cosmochim. Acta* **58,** 431–447.

Grossman L. (1972) Condensation in the primitive solar nebula. *Geochim. Cosmochim. Acta* **36,** 597–619.

Hart S. R. and Brooks C. (1977) The geochemistry and evolution of early Precambrian mantle. *Contr. Mineral. Petrol.* **61,** 109–128.

Hashimoto A. (1992) The effect of H_2O on volatilities of planet-forming major elements: I. Experimental determination of thermodynamic properties of Ca-, Al-, and Si-hydroxide gas molecules and its application to the solar nebula. *Geochim. Cosmochim. Acta* **56,** 511–532.

Hashimoto A. and Grossman L. (1987) Alteration of Al-rich inclusions inside amoeboid olivine aggregates in the Allende meteorite *Geochim. Cosmochim. Acta* **51,** 1685–1704.

Hinton R. W., Davis A. M., Scatena-Wachel D. E., Grossman L., and Draus R. J. (1988) A chemical and isotopic study of hibonite-rich refractory inclusions in primitive meteorites. *Geochim. Cosmochim. Acta* **52,** 2573–2598.

Hofmann A. W. (1980) Diffusion in natural silicate melts: A critical review. In *Physics of Magmatic Processes* (ed. R. B. Hargraves), pp. 385–417. Princeton University Press.

Hutcheon I. D. (1982) Ion probe magnesium isotopic measurements of Allende inclusions. *Amer. Chem. Soc. Symposium Series,* **176,** 95–128.

Hutcheon I. D. and Newton R. C. (1981) Mg isotopes, mineralogy, and mode of formation of secondary phases in C3 refractory inclusions. *Lunar Planet. Sci.* **XII,** 491–493 (abstr.).

Hutcheon I. D., Armstrong J. T., and Wasserburg G. J. (1987) Isotopic studies of Mg, Fe, Mo, Ru and W in Fremdlinge from Allende refractory inclusions. *Geochim. Cosmochim. Acta* **51,** 3175–3192.

Ireland T. R., Fahey A. J., and Zinner E. K. (1988) Trace-element abundances in hibonites from the Murchison carbonaceous chondrite: Constraints on high-temperature processes in the solar nebula. *Geochim. Cosmochim. Acta* **52,** 2841–2854.

Ireland T. R., Fahey A. J., and Zinner E. K. (1991) Hibonite-bearing microspherules: A new type of refractory inclusions with large isotopic anomalies. *Geochim. Cosmochim. Acta* **55,** 367–379.

Johnson M. L., Burnett D. S., and Woolum D. S. (1988) Relict refractory element rich phases in Type B CAI. *Meteoritics* **23,** 276 (abstr.).

Kennedy A. K. and Edwards D. A. (1991) Trace element partitioning during dissolution and crystallization in a closed system: Equations incorporating linear variation of partition coefficients in the crystallizing phases and convective or diffusive dissolution. *EOS, Trans. Amer. Geophys. Union* **72,** 577 (abstr.).

Kennedy A. K. and Hutcheon I. D. (1992) Chemical and isotopic constraints on the formation and crystallization of SA-1, a basaltic Allende plagioclase-olivine inclusion. *Meteoritics* **27,** 539–554.

Kennedy A. K., Beckett J. R., and Hutcheon I. D. (1988) The distribution of trace elements in an Allende Type B1 inclusion. *Meteoritics* **23,** 279 (abstr.).

Kennedy A. K., Beckett J. R., and Hutcheon I. D. (1990) Trace element and isotopic constraints on the formation and crystallization of a Type B1 CAI from Allende. *Lunar Planet. Sci. Conf.* **XXI,** 621–622 (abstr.).

Kennedy A. K., Lofgren G. E., and Wasserburg G. J. (1994) Trace-element partition coefficients for perovskite and hibonite in meteorite compositions. *Chem. Geol.* **117,** 379–390.

Kim C. J., Kim K. B., and Won D. Y. (1992) Oxygen diffusion paths and microcrack formation in the textured 1-2-3 regions of partial-melted Y-Ba-Cu-O oxide. *Mater. Lett.* **14,** 268–273.

Kuehner S. M., Laughlin J. R., Grossman L., Johnson M. L., and Burnett D. S. (1989a) Determination of trace element mineral/liquid partition coefficients in melilite and diopside by ion and electron microprobe techniques. *Geochim. Cosmochim. Acta* **53,** 3115–3130.

Kuehner S. M., Davis A. M., and Grossman L. (1989b) Identification of relict phases in a once-molten Allende inclusion. *Geophy. Res. Lett.* **16,** 775–778.

Lee T. (1988) Implications of isotopic anomalies for nucleosynthesis. In *Meteorites and the Early Solar System* (ed. J. F. Kerridge and M. S. Matthews), pp. 1063–1089. Univ. of Arizona Press.

Lesher C. E. and Walker D. (1986) Solution properties of silicate liquids from thermal diffusion experiments. *Geochim. Cosmochim. Acta* **50,** 1397–1411.

MacPherson G. J. and Davis A. M. (1993) A petrologic and ion microprobe study of a Vigarano Type B refractory inclusion: Evolution by multiple stages of alteration and melting. *Geochim. Cosmochim. Acta* **57,** 231–243.

MacPherson G. J. and Grossman L. (1981) A once-molten, coarse-grained, Ca-rich inclusion in Allende. *Earth. Planet. Sci. Lett.* **52,** 16–24.

MacPherson G. J., Paque J. M., Stolper E., and Grossman L. (1984) The origin and significance of reverse zoning in melilite from Allende Type B inclusions. *J. Geol.* **92,** 289–305.

MacPherson G. J., Crozaz G., and Lundberg L. L. (1989) The evolution of a complex type B Allende inclusion: An ion microprobe trace element study. *Geochim. Cosmochim. Acta* **53,** 2413–2427.

Mason B. and Taylor S. R. (1982) Inclusions in the Allende meteorite. *Smithsonian Contr. to Earth Sci.* **25,** 1–30.

McKeegan K. D., Leshin L. A., Russell S. S., and MacPherson G. J. (1996) In situ measurement of O isotopic anomalies in a type B Allende CAI. *Meteoritics Planet. Sci.* **31,** A86–A87 (abstr.).

Meeker G. P. (1990) Evidence for low temperature equilibration in Allende CAI. *Lunar Planet. Sci.* **XXI,** 781–782 (abstr.).

Meeker G. P. (1995) Constraints on formation processes of two coarse-grained calcium-aluminum-rich inclusions: A study of mantles, islands and cores. *Meteoritics* **30,** 71–84.

Meeker G. P., Wasserburg G. J., and Armstrong J. T. (1983) Replacement textures in CAI and implications regarding planetary metamorphism. *Geochim. Cosmochim. Acta* **47,** 707–721.

Morioka M. and Nagasawa H. (1991) Diffusion in single crystals of melilite: II. Cations. *Geochim. Cosmochim. Acta* **55,** 751–759.

Nagasawa H., Schreiber H. D., and Morris R. V. (1980) Experimental mineral/liquid partition coefficients of the rare earth elements (REE), Sc and Sr for perovskite, spinel and melilite. *Earth Planet. Sci. Lett.* **46,** 431–437.

Neumann H., Mead J., and Vitaliano C. J. (1954) Trace element variation during fractional crystallization as calculated from the distribution law. *Geochim. Cosmochim. Acta* **6,** 90–99.

Niederer F. R. and Papanastassiou D. A. (1984) Ca isotopes in refractory inclusions. *Geochim. Cosmochim. Acta* **48,** 1279–1293.

Paque J. M. (1990) Relict grains in a Ca-Al-rich inclusion from Allende. *Lunar Planet. Sci.* **XXI,** 932–933 (abstr.).

Podosek F. A., Zinner E. K., MacPherson G. J., Lundberg L. L., Brannon J. C., and Fahey A. J. (1991) Correlated study of initial $^{87}Sr/^{86}Sr$ and Al-Mg isotopic systematics and petrologic properties in a suite of refractory inclusions from the Allende meteorite. *Geochim. Cosmochim. Acta* **55,** 1083–1110.

Richter F. M. (1993) A method for determining activity-composition relations using chemical diffusion in silicate melts. *Geochim. Cosmochim. Acta* **57,** 2019–2032.

Ryerson F. J. and McKeegan K. D. (1994) Determination of oxygen self-diffusion in åkermanite, anorthite, diopside, and spinel: Implications for oxygen isotopic anomalies and thermal histories of Ca-Al-rich inclusions. *Geochim. Cosmochim. Acta* **58,** 3713–3734.

Sheng Y. J., Hutcheon I. D., and Wasserburg G. J. (1991) Origin of plagioclase-olivine inclusions in carbonaceous chondrites. *Geochim. Cosmochim. Acta* **55,** 581–599.

Sheng Y. J., Wasserburg G. J., and Hutcheon I. D. (1992) Self-diffusion of magnesium in spinel and in equilibrium melts: Constraints on flash heating of silicates. *Geochim. Cosmochim. Acta* **56,** 2535–2546.

Shimizu N. (1981) Trace element incorporation into growing augite phenocryst. *Nature* **289,** 575–577.

Simon S. B., Davis A. M., and Grossman L. (1990) "Relict" fassaite in Type B1 CAI's: Products of late-stage liquids? *Lunar Planet. Sci. Conf.* **XXI,** 1160–1161 (abstr.).

Simon S. B., Grossman L., and Davis A. M. (1991) Fassaite composition trends during crystallization of Allende Type B refractory inclusion melts. *Geochim. Cosmochim. Acta* **55,** 2635–2655.

Simon S. B., Kuehner S. M., Davis A. M., Grossman L., Johnson M. L., and Burnett D. S. (1994) Experimental studies of trace element partitioning in Ca, Al-rich compositions: Anorthite and perovskite. *Geochim. Cosmochim. Acta* **58,** 1507–1523.

Stolper E. (1982) Crystallization sequences of Ca-Al-rich inclusions from Allende: An experimental study. *Geochim. Cosmochim. Acta* **46,** 2159–2180.

Stolper E. and Paque J. M. (1986) Crystallization sequences of Ca-Al-rich inclusions from Allende: The effects of cooling rate and maximum temperature. *Geochim. Cosmochim. Acta* **50,** 1785–1806.

Wark D. A. (1981) The pre-alteration compositions of Allende Ca-Al-rich condensates. *Lunar Planet. Sci.,* **XII,** 1148–1149 (abstr.).

Wark D. A. and Lovering J. F. (1977) Marker events in the early evolution of the solar system: Evidence from rims on Ca-Al-rich inclusions in carbonaceous chondrites. *Proc. Lunar Sci. Conf. 8th,* 95–112.

Wark D. A. and Lovering J. F. (1982) The nature and origin of type B1 and B2 Ca-Al-rich inclusions in the Allende meteorite. *Geochim. Cosmochim. Acta* **46,** 2581–2594.

Watson E. B. and Liang Y. (1995) A simple model for sector zoning in slowly grown crystals: Implications for growth rate and lattice diffusion, with emphasis on accessory minerals in crustal rocks. *Amer. Mineral.* **80,** 1179–1187.

Zhang Y., Walker D., and Lesher C. E. (1989) Diffusive crystal dissolution. *Contr. Mineral Petrol.* **102,** 492–513.